

Linking thermodynamic correlation signatures and superconductivity in twisted trilayer graphene

Jesse C. Hoke,^{1,2,3,*} Yifan Li,^{1,2,3} Yuwen Hu,^{1,2,3} Julian May-Mann,¹ Kenji Watanabe,⁴ Takashi Taniguchi,⁵ Trithep Devakul,¹ Aaron Sharpe,^{1,3,†} and Benjamin E. Feldman^{1,2,3,‡}

¹*Department of Physics, Stanford University, Stanford, CA 94305, USA*

²*Geballe Laboratory for Advanced Materials, Stanford, CA 94305, USA*

³*Stanford Institute for Materials and Energy Sciences,
SLAC National Accelerator Laboratory, Menlo Park, CA 94025, USA*

⁴*Research Center for Electronic and Optical Materials,
National Institute for Materials Science, 1-1 Namiki, Tsukuba 305-0044, Japan*

⁵*Research Center for Materials Nanoarchitectonics,
National Institute for Materials Science, 1-1 Namiki, Tsukuba 305-0044, Japan*

Twisted graphene multilayers exhibit strong electronic correlations, which manifest in a range of experimental signatures. Yet how these signatures relate to each other and the microscopic ground states—and how twist angle and band structure reshape them—remains poorly understood. Here we study this interplay by correlating local thermodynamic and transport measurements in a twisted trilayer graphene (TTG) sample with unequal angles and flat electronic bands. We use a scanning single-electron transistor to map the impact of electron-electron interactions in a region of the sample where the local twist angle evolves smoothly. We observe gapped correlated insulators and a “sawtooth” in electronic compressibility, both exhibiting pronounced electron-hole (e - h) asymmetry with distinct “magic” angles for conduction and valence bands. Subsequent transport measurements in the same region reveal robust superconductivity with a similar e - h asymmetry. Our measurements indicate that superconductivity is not directly tied to the correlated insulators. Instead, its critical temperature correlates closely with the strength of the sawtooth in compressibility, suggesting a common origin or link between the two. By combining a local probe with transport measurements, we uncover connections between superconductivity and thermodynamic correlation signatures that are not apparent from either technique in isolation, highlighting the power of our dual approach and establishing their dependence on interlayer twist angles in TTG.

INTRODUCTION

Understanding how electron-electron interactions generate competing and coexisting orders is a longstanding challenge in condensed matter physics. Due to their high degree of tunability, moiré flat bands [1–3] are an excellent testbed for realizing and probing correlated states. The first discovered example, magic-angle twisted bilayer graphene (MATBG) [4], hosts a wide range of interaction-driven effects, including correlated insulators [5–8], superconductivity [6, 7, 9–11], and a sawtooth in compressibility as a function of filling [12–16]. Transport experiments across different devices have used Coulomb screening to explore the relationship between superconductivity and the correlated insulators, finding that superconductivity could persist even in the absence of proximate correlated insulating states, or vice versa [17–22]. However, a detailed understanding of the origin of superconductivity and its relation to other correlated ground states remains elusive. Establishing the link between different correlation signatures, including those seen via other means such as thermodynamic mea-

surements, is an important goal but has been hindered by sample-to-sample variability in twist angle, dielectric environment, strain, and/or disorder.

The same signatures of strong correlations are commonly found in other twisted graphene multilayers [23–32]. These structures both expand the accessible parameter space and enable further modification of the electronic structure by the interference between multiple moiré patterns, providing new opportunities to probe strongly correlated phenomena with enhanced tunability. The simplest example is twisted trilayer graphene (TTG): three graphene sheets with two independent interlayer twist angles θ_{12} and θ_{23} (here we assume $|\theta_{12}| \leq |\theta_{23}|$ without loss of generality). Calculations predict that TTG hosts a “magic continuum” of angle combinations exhibiting flat bands [33–36]. Along this continuum, the resulting correlated phenomena depend sensitively on the magnitude and relative sign (helical vs. alternating) of the twist angles. Aside from work on mirror-symmetric magic-angle twisted trilayer graphene (MATTG; $\theta_{12} = -\theta_{23} \approx 1.55^\circ$) [23–26, 30, 37–43], only a handful of studies have explored other twist angle combinations along the magic continuum [29, 44–46]. The broader TTG phase diagram offers opportunities to probe how varying twist angles and layer numbers influence signatures of correlations—revealing whether the same generic features persist and any correspondence between them.

Here, we report local thermodynamic and charge

* jchoke@hrl.com; Current Address: HRL Laboratories, LLC, 3011 Malibu Canyon Road, Malibu, California 90265, USA

† aaron.sharpe@stanford.edu

‡ bef@stanford.edu

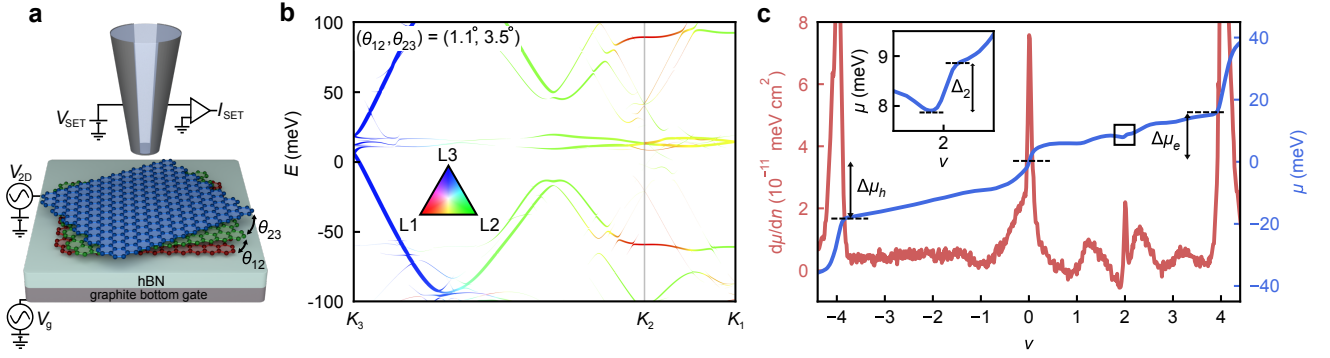


FIG. 1. **Twisted trilayer graphene (TTG) with $\theta_{12}/\theta_{23} \approx 1/3$.** **a**, Schematic of the measurement setup and device (Methods). Three graphene layers are sequentially twisted in the same direction (helical stacking), with a twist angle ratio near $\theta_{12}/\theta_{23} = 1/3$. **b**, Calculated spectral function of TTG along a path between the K points of each layer for $(\theta_{12}, \theta_{23}) = (1.1^\circ, 3.5^\circ)$. **c**, Inverse electronic compressibility $d\mu/dn$ (red) and chemical potential μ (blue) as a function of moiré filling factor ν associated with layers 1 and 2 at a location where $\theta_{12} = 1.10^\circ$ and measured at temperature $T = 330$ mK. We estimate $\theta_{23} \approx 3.45^\circ$ at this location by measuring the renormalized Fermi velocity v_F^* of the Dirac-like cone (Fig. ED2; Methods). $\Delta\mu_{e(h)}$ is defined as the total change in the chemical potential to fill the conduction (valence) bands. Inset: The step in μ at $\nu = 2$ defines the gap size Δ_2 of the correlated insulator.

transport measurements within a TTG sample that lies near the magic continuum with mismatched twist angles $\theta_{12}/\theta_{23} \approx 1/3$ (Fig. 1a). Electronic compressibility measurements with a single-electron transistor (SET) microscope show correlated insulators and a sawtooth in compressibility which are maximized at different interlayer twists for the conduction and valence bands. Transport measurements in the same region reveal robust superconducting phases with an e - h asymmetry in the critical temperature that closely mirrors the strength of the sawtooth in inverse compressibility, but not the correlated insulators. Our work provides a direct comparison of thermodynamic and transport signatures, including their joint evolution with twist angle, while avoiding confounding factors inherent in cross-device studies. We shed new light on the relationship between superconductivity and other correlation effects, simultaneously clarifying which structural and electronic parameters dominate electronic behavior in twisted graphene multilayers.

ELECTRONIC STRUCTURE

We first describe the electronic characteristics relevant to our TTG device. Figure 1b shows the calculated spectral function along the path $K_3 \rightarrow K_2 \rightarrow K_1$ for $(\theta_{12}, \theta_{23}) = (1.1^\circ, 3.5^\circ)$ (Methods; see Fig. ED1 for calculations at other twist angle combinations). The colors represent the relative weight on each respective graphene layer (inset of Fig. 1b). The flat bands predominately originate from the strong hybridization between layers 1 and 2 due to their small interlayer twist. Layers 2 and 3 are more weakly coupled at low energies, resulting in a Dirac-like cone centered at K_3 predominantly associated with layer 3. It has a renormalized Fermi velocity $v_F^* < v_F^0$, where v_F^0 is the Fermi velocity of bare graphene.

The result is an electronic system with coexisting light and heavy fermions where correlation effects are anticipated when the Fermi energy lies within the flat bands.

We experimentally probe the electronic structure and resulting ground states by measuring the local inverse electronic compressibility $d\mu/dn$ with a high-resolution scanning SET (Methods). Representative traces of $d\mu/dn$ and the corresponding chemical potential μ as a function of filling at a fixed position are shown in Fig. 1c. We identify the local twist angle $\theta_{12} = 1.10^\circ$ from the density n of the two largest incompressible peaks, which are associated with full-filling ($\nu = \pm 4$) of the moiré unit cell created by layers 1 and 2 (Methods). We estimate $\theta_{23} \approx 3.45^\circ$ based on the extracted Fermi velocity v_F^* of the Landau levels from the Dirac-like cone in a magnetic field (Methods and Fig. ED2). At intermediate fillings, we find a sharp incompressible state at $\nu = 2$, indicating a correlated insulator with a gap $\Delta_2 = 1$ meV, as well as more slowly varying sawtooth-like oscillations in $d\mu/dn$ that occur between $0 < \nu < 4$. Both of these features closely match ubiquitous signatures of strong correlations reported in other twisted graphene systems [5–8, 12–14, 23, 25, 30, 47].

MAPPING TWIST-DEPENDENT SIGNATURES OF INTERACTION EFFECTS

To characterize the twist angle dependence of the correlations in TTG, we map $d\mu/dn$ as a function of spatial position (Fig. 2a; see Fig. ED3 for additional line cuts). Along this line cut, θ_{12} varies smoothly from $\theta_{12} \approx 1^\circ$ to $\theta_{12} \approx 1.4^\circ$ over a span of about $4 \mu\text{m}$. Strong interactions, indicated by the presence of correlation-driven gaps at $\nu = \pm 2$ and/or a sawtooth in compressibility, persist over a range of twist angles $1.03^\circ < \theta_{12} < 1.24^\circ$. This range is consistent with the theoretically predicted magic

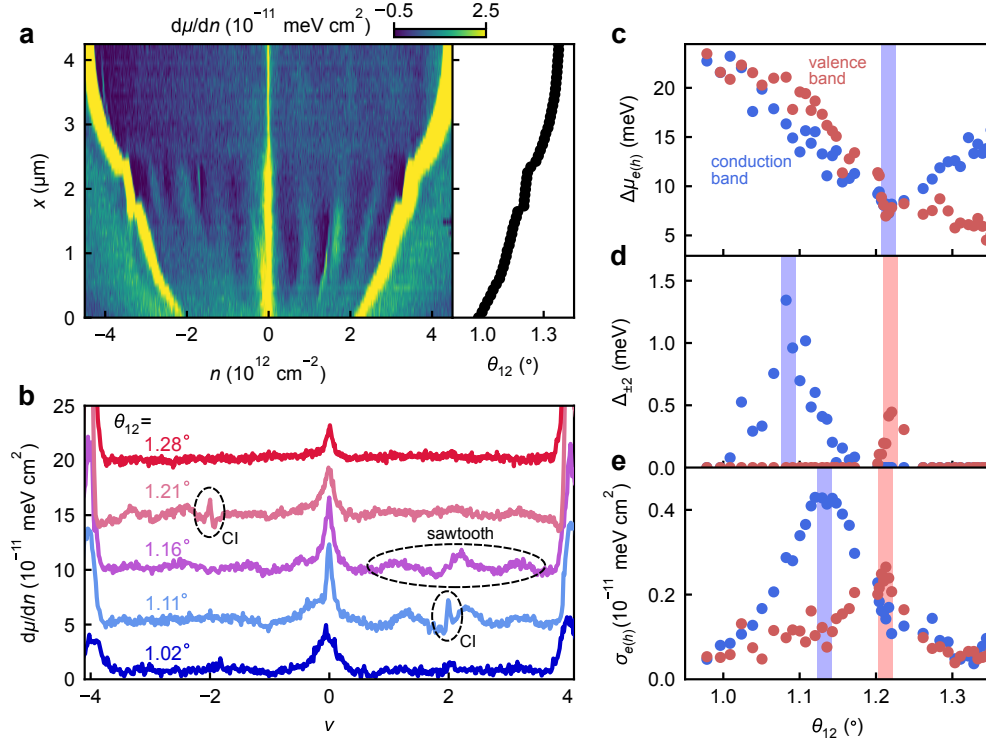


FIG. 2. **Mapping twist-dependent interaction strength and e - h asymmetry.** **a**, Spatial dependence of $d\mu/dn$ as a function of carrier density n at $T = 1.6$ K (left panel) and the corresponding local twist angle θ_{12} (right panel). **b**, $d\mu/dn$ as a function of ν for select twist angles from the line cut in **a**. The correlated insulators at $\nu = \pm 2$ and the sawtooth of $d\mu/dn$ are circled with black dashed lines. Curves are offset for clarity. **c**, The change in the chemical potential across the conduction band ($\Delta\mu_e$; blue), and the valence band ($\Delta\mu_h$; red) as a function of θ_{12} . **d**, The gap of the correlated insulator $\Delta_{\pm 2}$ at $\nu = \pm 2$ (blue and red, respectively), as a function of θ_{12} . **e**, The strength of the sawtooth (Methods) in $d\mu/dn$ for electron (hole) doping $\sigma_{e(h)}$ (blue and red, respectively), as a function of θ_{12} .

continuum of angles for TTG where single-particle bandwidths are minimized for our θ_{23} [33–35]. The data reveal that the locations where correlations are maximized for hole and electron doping differ, indicating distinct effective magic angles for the valence and conduction bands (Fig. 2b). While differences between the valence and conduction band behaviors are frequently observed in twisted graphene samples, our spatially resolved measurements reveal that both bands can host correlations of similar strength, yet the detailed conditions that optimize interaction effects within each band are different.

To quantify the θ_{12} dependence and the e - h asymmetry, we extract three key parameters from the line cut in Fig. 2a. The first is the change in chemical potential $\Delta\mu_{e(h)}$ to fully fill the conduction (valence) band, depicted schematically in Fig. 1c. The second is the gap size $\Delta_{\pm 2}$ of the correlated insulators at $\nu = \pm 2$ (inset of Fig. 1c; Methods). Third, we quantify the strength of the sawtooth in inverse compressibility as $\sigma_{e(h)}$, the standard deviation of $d\mu/dn$ between $0.5 < |\nu| < 3.5$ for electron and hole doping, respectively. A small (large) $\sigma_{e(h)}$ indicates a weak/nonexistent (strong) sawtooth variation. When calculating $\sigma_{e(h)}$, a filter is applied to smooth the peaks in $d\mu/dn$ associated with the $\nu = \pm 2$ correlated insulators, ensuring these effects can be evaluated inde-

pendently (Methods and Fig. ED4).

We plot $\Delta\mu_{e(h)}$, $\Delta_{\pm 2}$, and $\sigma_{e(h)}$ as a function of θ_{12} in Fig. 2c-e, respectively. Interaction strength, as quantified by both $\Delta_{\pm 2}$ and $\sigma_{e(h)}$, is maximized at different θ_{12} for conduction and valence bands. The θ_{12} where $\Delta_{\pm 2}$ and $\sigma_{e(h)}$ are maximal are not coincident with the minimum of $\Delta\mu_{e(h)}$, as might be expected. Note, however, that $\Delta\mu$ is not equivalent to the non-interacting bandwidth because interactions significantly modify the band structure as the bands are filled, enhancing the many-body interacting $\Delta\mu$ extracted here [8, 48, 49]. In addition, σ_e and Δ_2 are themselves maximized at different θ_{12} . The fact that these different features do not evolve together as a function of twist angle shows that the detailed conditions required to produce each are not identical.

While 1D spatial line cuts provide a concrete quantitative understanding of how the electronic character varies with θ_{12} , a natural question is the extent to which other microscopic parameters, such as local variations in θ_{23} or strain, may influence the resulting electronic properties. To address this, we conduct local measurements of $d\mu/dn$ spanning a $1 \times 1 \mu\text{m}^2$ area where θ_{12} varies between 1.07° and 1.22° (Fig. ED5), extracting $\Delta\mu_f$ (the sum of $\Delta\mu_e$ and $\Delta\mu_h$), Δ_2 , and $\sigma_{e(h)}$ at each pixel. θ_{12} is

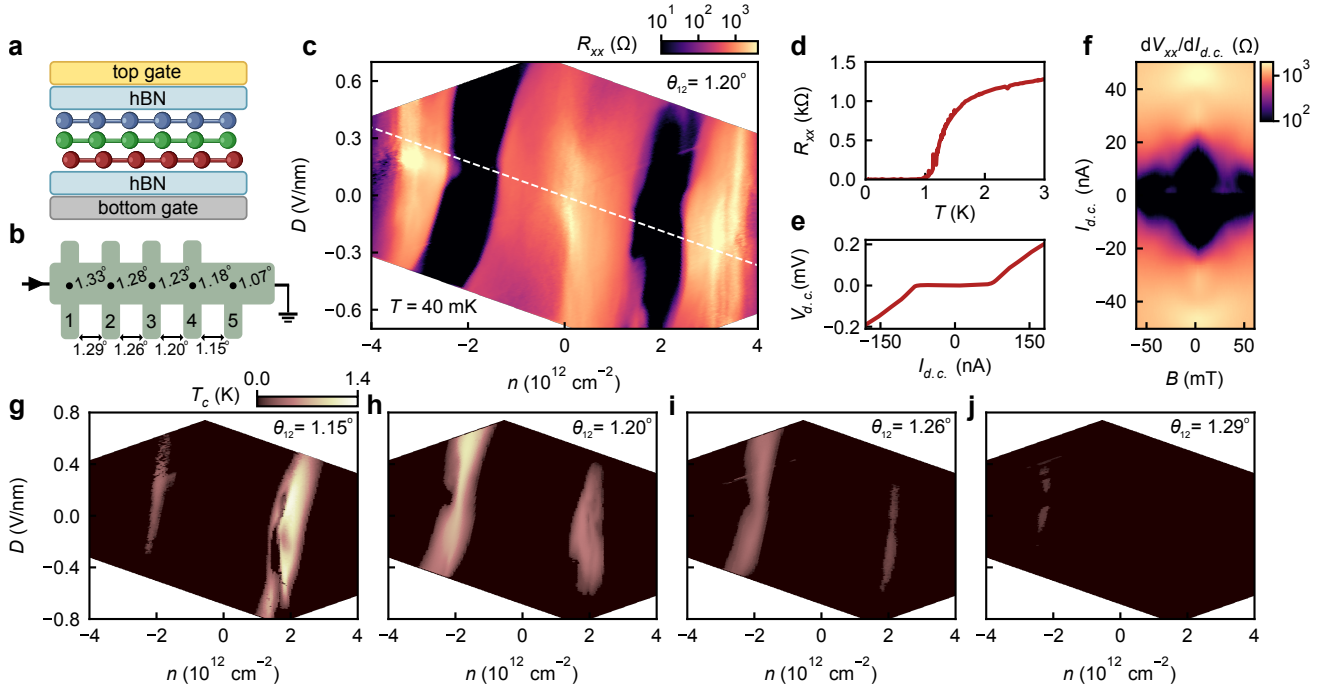


FIG. 3. Dual-gated transport and superconductivity. **a-b**, Schematic of the dual-gated device structure (**a**) and its Hall bar geometry (**b**). Contacts 1-5 are labeled, along with the observed twist angles θ_{12} between contact pairs as measured in transport (bottom), and from local compressibility measurements in the Hall bar (black dots; see Fig. ED3). **c**, Longitudinal resistance R_{xx} between contacts 3 and 4 as a function of n and displacement field D . The white dashed line corresponds to where the top gate voltage $V_t = 0$, which most closely approximates the conditions of SET measurements. **d**, R_{xx} as a function of T for contacts 3-4 at $n = -1.69 \times 10^{12} \text{ cm}^{-2}$ and $D = 0.50 \text{ V/nm}$. **e**, d.c. voltage $V_{d.c.}$ as a function of d.c. current $I_{d.c.}$ for contacts 3-4 at $T = 40 \text{ mK}$, $n = -1.69 \times 10^{12} \text{ cm}^{-2}$, and $D = 0.50 \text{ V/nm}$. **f**, $dV_{xx}/dI_{d.c.}$ as a function of $I_{d.c.}$ and perpendicular magnetic field B for contacts 3-4 at $T = 40 \text{ mK}$, $n = -2.35 \times 10^{12} \text{ cm}^{-2}$, and $D = -0.26 \text{ V/nm}$. Oscillations in the critical current as a function of B are emblematic of phase coherent transport. **g-j**, Critical temperature T_c (defined as 10% of the normal state resistance; Methods) as a function of n and D for each contact pair.

the dominant determinant of electronic behavior, consistent with its direct relation to the flat bands. However, the data reveal systematic spatial variability in each of these parameters even as θ_{12} remains fixed (Fig. ED5h-k), clearly demonstrating that θ_{23} and/or local strain can play a secondary, but non-negligible role in modifying the electronic structure. Although the specific microscopic origins of this spatial dependence are difficult to determine conclusively, we speculate that the observed variations are more likely to result from spatial variability in θ_{23} than by changes in local strain (Methods).

SUPERCONDUCTIVITY

Having established the local twist angle dependence of thermodynamic correlation signatures, we next measure transport in the same area of the device for direct comparison. To do so, we patterned a large portion of the SET-characterized region into a Hall bar, using a deposited metal top gate as a hard etch mask (Fig. ED6; Methods). The newly dual gated architecture allows independent control of the carrier density n and displace-

ment field D (Fig. 3a). We oriented the long axis of the Hall bar along the local gradient in θ_{12} as measured by SET (Fig. ED3). This enables us to correlate signatures in transport with angle-resolved features in electronic compressibility from the scanning SET. The twist angles θ_{12} determined from transport (Methods) quantitatively match those measured with the scanning SET in the vicinity of each contact pair (Fig. 3b, Fig. ED3), indicating that the additional fabrication procedures did not meaningfully change the interlayer twists within the heterostructure.

Figure 3c shows the longitudinal resistance R_{xx} as a function of n and D between contacts 3 and 4, whose $\theta_{12} = 1.20^\circ$. At temperature $T = 40 \text{ mK}$, we observe two large superconducting pockets of zero resistance upon both electron and hole doping. The superconductivity is confirmed by standard temperature dependence, non-linear I - V characteristics, and magnetic field measurements that exhibit evidence of phase coherent transport through oscillations in the critical current (Fig. 3d-f). The regions of superconductivity exhibit a slight tilt as n and D are varied (Fig. 3c), which likely originates from changes in the occupation of the Dirac-like band from the weakly coupled third layer as D tunes the layer po-

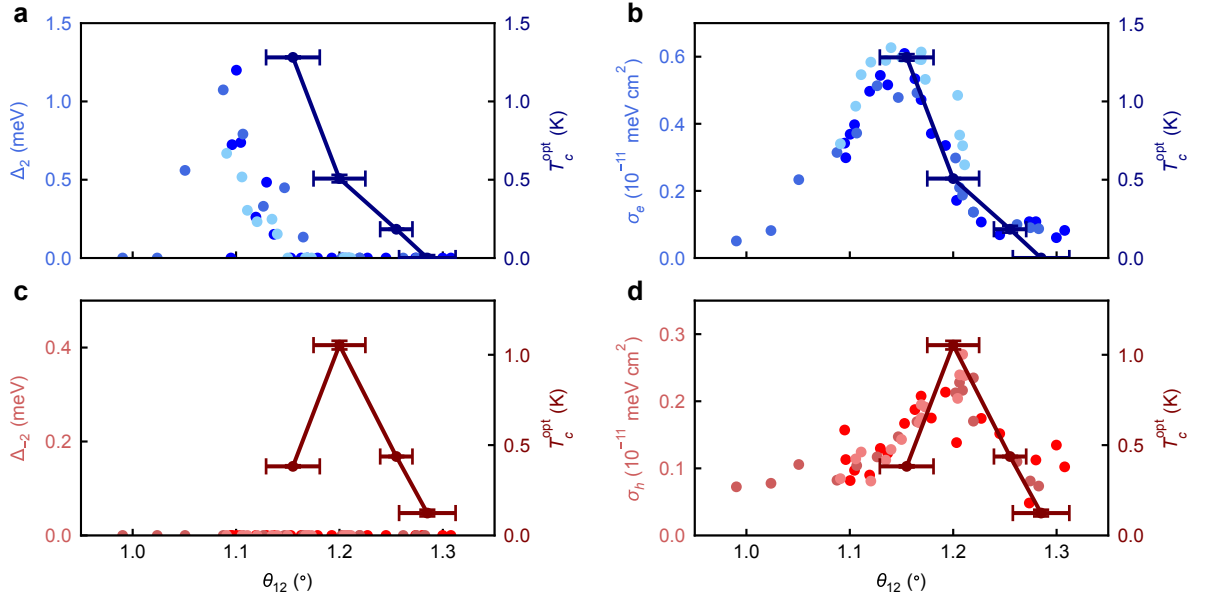


FIG. 4. **Comparison of correlation signatures in compressibility and superconductivity in transport.** **a**, Δ_2 , as measured by local compressibility, and critical temperature at optimal doping T_c^{opt} , as measured by transport, as a function of θ_{12} for the conduction band (electron doping). **b**, σ_e and T_c^{opt} as a function of θ_{12} for the conduction band. **c-d**, Same as **a-b**, but for the valence band (hole doping). For each panel distinct dot colors represent different line cuts (line cuts 2-4 in Fig. ED3) taken with the scanning SET that overlap with the Hall bar. Horizontal and vertical error bars respectively represent the uncertainty in θ_{12} as measured in transport and the uncertainty in the extraction of T_c^{opt} . Similar comparisons based on other spatially resolved datasets in distinct locations are shown in Fig. ED9 and Fig. ED10, which are consistent with the data shown here.

tentials. The transport features do not all evolve under variations in n and D with the characteristic S-shape (Fig. ED7) that was previously seen when layer 3 becomes fully decoupled for $\theta_{23} \gtrsim 5^\circ$ [44]. This indicates some hybridization of layer 3 with the other two, which is consistent with the observation of a renormalized Fermi velocity in the scanning SET measurements (Fig. ED2).

Measurements across different contact pairs demonstrate that superconducting regions persist as θ_{12} varies from 1.15° to 1.29° (Fig. ED7). The superconductivity also exhibits e - h asymmetry as a function of θ_{12} . This is evident from the measured critical temperature T_c (defined to be the temperature where R_{xx} reaches 10% of the normal state resistance; Methods) of the electron- and hole-doped superconducting phases as a function of n and D (Fig. 3g-j). In particular, the electron-doped superconductor exhibits its maximum critical temperature of 1.28 K at $\theta_{12} = 1.15^\circ$. Both the extent of the superconducting region and T_c generally decrease with increasing θ_{12} for electrons. In contrast, for hole-doping, superconductivity reaches its maximum critical temperature of 1.05 K in the contact pair with $\theta_{12} = 1.20^\circ$. The extent of the hole-doped superconducting region and the T_c generally decrease as θ_{12} is further increased or decreased. Thus, superconductivity is optimized at a larger θ_{12} for holes than for electrons, much like the signatures of interactions in local inverse compressibility.

COMPARING COMPRESSIBILITY AND TRANSPORT

We next directly compare the correlation signatures measured from compressibility with the superconductivity measured via transport. In Fig. 4a-b we plot Δ_2 and σ_e , respectively, as a function of θ_{12} (left axis) alongside the critical temperature T_c^{opt} at optimal doping and displacement field of the electron-doped superconductor for each contact pair (right axis). The corresponding results for Δ_{-2} , σ_h , and T_c^{opt} of the hole-doped superconductor are shown in Fig. 4c-d. For the compressibility measurements, the dot colors denote different spatial line cuts taken with the SET microscope that overlap with the Hall bar (Fig. ED3). For reference, we also include a comparison of individual traces of $d\mu/dn$ and R_{xx} in Fig. ED8. Note that we do not include the data of Fig. 2 here, which is adjacent to but outside the Hall bar (Fig. ED3); an equivalent comparison with that data is shown in Fig. ED9.

The twist angle dependencies of $\Delta_{\pm 2}$ and T_c^{opt} do not identically overlap. With decreasing twist angle for electron-doping, we observe that superconductivity onsets at a higher twist angle than Δ_2 , forming a window of θ_{12} where $T_c^{\text{opt}} > 0$ while $\Delta_2 = 0$. Notably, for the valence band, no thermodynamically gapped state is observed at $\nu = -2$ within the defined region of the Hall bar (Fig. ED3), yet $T_c^{\text{opt}} > 0$ for every contact pair. These observations are consistent with a picture in which the

correlated insulator and superconducting phases are independent or competing [17–19].

In contrast, comparing $\sigma_{e(h)}$ with T_c^{opt} uncovers a markedly closer correlation, with the relative strength of each signature displaying dependence on θ_{12} with near-identical scaling. This correlation is present not only for the compressibility data shown here, but also that from the line cut in Fig. 2 (Fig. ED9) and the $1 \times 1 \mu\text{m}^2$ area of the sample (Fig. ED10). Taken together, the close correlation between $\sigma_{e(h)}$ and T_c^{opt} suggests a deeper relationship between the two, which we discuss below.

DISCUSSION

The direct link between the strength of superconductivity and the sawtooth in compressibility raises interesting questions on the possible nature of the superconductivity. Recent experiments indicate that the sawtooth in compressibility in MATBG can be attributed to the redistribution of light and heavy charge carriers as the system is doped [49–51]. While itinerant conduction carriers are necessary for superconductivity in MATBG, it is possible heavy carriers and the interplay between the two charge sectors could also contribute [52], in analogy to heavy fermion superconductors [53]. Alternatively, it is possible that both signatures are independently maximized by the same underlying conditions. For example, a large density of states is favorable for superconductivity [54], and it can also lead to Stoner-induced transitions in the occupation of distinct carriers. Our work motivates further theoretical efforts to examine why the sawtooth and superconductivity correlate so closely.

While our system has an additional coexisting dispersive Dirac-like band from the third layer, similar models of light and heavy fermions have been extended to systems hosting coexisting flat and dispersive Dirac-like bands [55]. In our experiment, superconductivity persists over a wide range of D , including where the filling of the Dirac-like band is negligible, suggesting that its carriers are not a prerequisite for superconductivity. However, we note that the extent of superconductivity is often markedly affected by the applied displacement field (Fig. 3g-j), suggesting states from the quasi-decoupled layer and/or changes in band structure can play a role.

A detailed understanding of how superconductivity is modified by the filling of the Dirac-like band or the D -dependent hybridization between the coexisting flat and dispersive bands remains an open question and topic for future study.

We also report regions within the sample where both electron and hole-doped superconductors exist in the absence of proximate correlated insulators, consistent with the superconductors and correlated insulators being either competing or independent phases. The correlated insulators at $\nu = \pm 2$ also appear to be more fragile, present only in a subset of the parameter space where we observe a sawtooth in $d\mu/dn$. This fragility is particularly pronounced for the correlated insulator at $\nu = -2$, which is only observed in a small region of the sample (Fig. ED3). These observations align with proposals that the ordered phases at integer filling are inherently more delicate [56–60], exhibiting greater sensitivity to strain, θ_{23} , and/or disorder than the sawtooth in $d\mu/dn$, and, evidently, superconductivity.

The above insights were possible because we used local SET microscopy to first identify and characterize a region of a TTG sample with a range of slowly and smoothly varying θ_{12} of interest. Subsequently leveraging this knowledge to inform the placement of a Hall bar device then enabled a direct comparison between compressibility and transport without the confounding factors of sample-to-sample variations. Our work demonstrates that θ_{12} is the key parameter determining strongly correlated behavior near $\theta_{12}/\theta_{23} \approx 1/3$ and links distinct thermodynamic and transport signatures in TTG. An interesting direction for future work is to determine whether the observed correlation relations persist across other regions of the TTG magic continuum and in other twisted graphene multilayers. More generally, this “local-to-global” approach is broadly applicable to elucidate the nature of correlated ground states in a variety of other van der Waals systems, which often host intertwined orders. Employing joint complementary experimental probes, as we have exemplified here, is a powerful route to disentangle the nature of correlated phases and discover relationships between them.

Note added: While finalizing this manuscript, we became aware of a related work that also observed superconductivity in helically-twisted TTG with $\theta_{12}/\theta_{23} \approx 1/3$ [61].

-
- [1] E. Y. Andrei and A. H. MacDonald, Graphene bilayers with a twist, *Nature Materials* **19**, 1265 (2020).
 - [2] L. Balents, C. R. Dean, D. K. Efetov, and A. F. Young, Superconductivity and strong correlations in moiré flat bands, *Nature Physics* **16**, 725 (2020).
 - [3] K. F. Mak and J. Shan, Semiconductor moiré materials, *Nature Nanotechnology* **17**, 686 (2022).
 - [4] R. Bistritzer and A. H. MacDonald, Moiré bands in twisted double-layer graphene, *Proceedings of the Na-*

tional Academy of Sciences **108**, 12233 (2011).

- [5] Y. Cao, V. Fatemi, A. Demir, S. Fang, S. L. Tomarken, J. Y. Luo, J. D. Sanchez-Yamagishi, K. Watanabe, T. Taniguchi, E. Kaxiras, *et al.*, Correlated insulator behaviour at half-filling in magic-angle graphene superlattices, *Nature* **556**, 80 (2018).
- [6] M. Yankowitz, S. Chen, H. Polshyn, Y. Zhang, K. Watanabe, T. Taniguchi, D. Graf, A. F. Young, and C. R. Dean, Tuning superconductivity in twisted bilayer graphene,

- Science **363**, 1059 (2019).
- [7] X. Lu, P. Stepanov, W. Yang, M. Xie, M. A. Aamir, I. Das, C. Urgell, K. Watanabe, T. Taniguchi, G. Zhang, *et al.*, Superconductors, orbital magnets and correlated states in magic-angle bilayer graphene, *Nature* **574**, 653 (2019).
 - [8] J. Yu, B. A. Foutty, Y. H. Kwan, M. E. Barber, K. Watanabe, T. Taniguchi, Z.-X. Shen, S. A. Parameswaran, and B. E. Feldman, Spin skyrmion gaps as signatures of strong-coupling insulators in magic-angle twisted bilayer graphene, *Nature Communications* **14**, 6679 (2023).
 - [9] Y. Cao, V. Fatemi, S. Fang, K. Watanabe, T. Taniguchi, E. Kaxiras, and P. Jarillo-Herrero, Unconventional superconductivity in magic-angle graphene superlattices, *Nature* **556**, 43 (2018).
 - [10] H. S. Arora, R. Polski, Y. Zhang, A. Thomson, Y. Choi, H. Kim, Z. Lin, I. Z. Wilson, X. Xu, J.-H. Chu, *et al.*, Superconductivity in metallic twisted bilayer graphene stabilized by wse_2 , *Nature* **583**, 379 (2020).
 - [11] Y. Cao, D. Rodan-Legrain, J. M. Park, N. F. Yuan, K. Watanabe, T. Taniguchi, R. M. Fernandes, L. Fu, and P. Jarillo-Herrero, Nematicity and competing orders in superconducting magic-angle graphene, *science* **372**, 264 (2021).
 - [12] U. Zondiner, A. Rozen, D. Rodan-Legrain, Y. Cao, R. Queiroz, T. Taniguchi, K. Watanabe, Y. Oreg, F. von Oppen, A. Stern, *et al.*, Cascade of phase transitions and dirac revivals in magic-angle graphene, *Nature* **582**, 203 (2020).
 - [13] J. Yu, B. A. Foutty, Z. Han, M. E. Barber, Y. Schattner, K. Watanabe, T. Taniguchi, P. Phillips, Z.-X. Shen, S. A. Kivelson, *et al.*, Correlated hofstadter spectrum and flavour phase diagram in magic-angle twisted bilayer graphene, *Nature Physics* **18**, 825 (2022).
 - [14] Y. Saito, F. Yang, J. Ge, X. Liu, T. Taniguchi, K. Watanabe, J. Li, E. Berg, and A. F. Young, Isospin pomeranchuk effect in twisted bilayer graphene, *Nature* **592**, 220 (2021).
 - [15] A. Rozen, J. M. Park, U. Zondiner, Y. Cao, D. Rodan-Legrain, T. Taniguchi, K. Watanabe, Y. Oreg, A. Stern, E. Berg, *et al.*, Entropic evidence for a pomeranchuk effect in magic-angle graphene, *Nature* **592**, 214 (2021).
 - [16] A. T. Pierce, Y. Xie, J. M. Park, E. Khalaf, S. H. Lee, Y. Cao, D. E. Parker, P. R. Forrester, S. Chen, K. Watanabe, *et al.*, Unconventional sequence of correlated chern insulators in magic-angle twisted bilayer graphene, *Nature Physics* **17**, 1210 (2021).
 - [17] Y. Saito, J. Ge, K. Watanabe, T. Taniguchi, and A. F. Young, Independent superconductors and correlated insulators in twisted bilayer graphene, *Nature Physics* **16**, 926 (2020).
 - [18] P. Stepanov, I. Das, X. Lu, A. Fahimniya, K. Watanabe, T. Taniguchi, F. H. Koppens, J. Lischner, L. Levitov, and D. K. Efetov, Untying the insulating and superconducting orders in magic-angle graphene, *Nature* **583**, 375 (2020).
 - [19] X. Liu, Z. Wang, K. Watanabe, T. Taniguchi, O. Vafeek, and J. Li, Tuning electron correlation in magic-angle twisted bilayer graphene using coulomb screening, *Science* **371**, 1261 (2021).
 - [20] X. Gao, A. Jimeno-Pozo, P. A. Pantaleon, E. Codecido, D. L. Sharifi, Z. Zhang, Y. Liu, K. Watanabe, T. Taniguchi, M. W. Bockrath, *et al.*, Double-edged role of interactions in superconducting twisted bilayer graphene, *arXiv preprint arXiv:2412.01578* (2024).
 - [21] J. Barrier, L. Peng, S. Xu, V. Fal'ko, K. Watanabe, T. Taniguchi, A. Geim, S. Adam, and A. I. Berdyugin, Coulomb screening of superconductivity in magic-angle twisted bilayer graphene, *arXiv preprint arXiv:2412.01577* (2024).
 - [22] Y. Wang, J. Zhu, G. W. Burg, A. Swain, K. Watanabe, T. Taniguchi, Y. Zheng, A. H. MacDonald, and E. Tutuc, Independently tunable flat bands and correlations in a graphene double moiré system, *Physical Review Letters* **134**, 096204 (2025).
 - [23] J. M. Park, Y. Cao, K. Watanabe, T. Taniguchi, and P. Jarillo-Herrero, Tunable strongly coupled superconductivity in magic-angle twisted trilayer graphene, *Nature* **590**, 249 (2021).
 - [24] Z. Hao, A. Zimmerman, P. Ledwith, E. Khalaf, D. H. Najafabadi, K. Watanabe, T. Taniguchi, A. Vishwanath, and P. Kim, Electric field-tunable superconductivity in alternating-twist magic-angle trilayer graphene, *Science* **371**, 1133 (2021).
 - [25] X. Liu, N. J. Zhang, K. Watanabe, T. Taniguchi, and J. Li, Isospin order in superconducting magic-angle twisted trilayer graphene, *Nature Physics* **18**, 522 (2022).
 - [26] Y. Cao, J. M. Park, K. Watanabe, T. Taniguchi, and P. Jarillo-Herrero, Pauli-limit violation and re-entrant superconductivity in moiré graphene, *Nature* **595**, 526 (2021).
 - [27] Y. Zhang, R. Polski, C. Lewandowski, A. Thomson, Y. Peng, Y. Choi, H. Kim, K. Watanabe, T. Taniguchi, J. Alicea, *et al.*, Promotion of superconductivity in magic-angle graphene multilayers, *Science* **377**, 1538 (2022).
 - [28] J. M. Park, Y. Cao, L.-Q. Xia, S. Sun, K. Watanabe, T. Taniguchi, and P. Jarillo-Herrero, Robust superconductivity in magic-angle multilayer graphene family, *Nature Materials* **21**, 877 (2022).
 - [29] A. Uri, S. C. de la Barrera, M. T. Randeria, D. Rodan-Legrain, T. Devakul, P. J. Crowley, N. Paul, K. Watanabe, T. Taniguchi, R. Lifshitz, *et al.*, Superconductivity and strong interactions in a tunable moiré quasicrystal, *Nature* **620**, 762 (2023).
 - [30] A. T. Pierce, Y. Xie, J. M. Park, Z. Cai, K. Watanabe, T. Taniguchi, P. Jarillo-Herrero, and A. Yacoby, Tunable interplay between light and heavy electrons in twisted trilayer graphene, *Nature Physics* , 1 (2025).
 - [31] G. Chen, A. L. Sharpe, E. J. Fox, Y.-H. Zhang, S. Wang, L. Jiang, B. Lyu, H. Li, K. Watanabe, T. Taniguchi, *et al.*, Tunable correlated chern insulator and ferromagnetism in a moiré superlattice, *Nature* **579**, 56 (2020).
 - [32] X. Zhang, K.-T. Tsai, Z. Zhu, W. Ren, Y. Luo, S. Carr, M. Lusk, E. Kaxiras, and K. Wang, Correlated insulating states and transport signature of superconductivity in twisted trilayer graphene superlattices, *Physical review letters* **127**, 166802 (2021).
 - [33] Z. Zhu, S. Carr, D. Massatt, M. Lusk, and E. Kaxiras, Twisted trilayer graphene: A precisely tunable platform for correlated electrons, *Physical review letters* **125**, 116404 (2020).
 - [34] C. Yang, J. May-Mann, Z. Zhu, and T. Devakul, Multi-moiré trilayer graphene: lattice relaxation, electronic structure, and magic angles, *Physical Review B* **110**, 115434 (2024).
 - [35] D. Foo, Z. Zhan, M. M. Al Ezzi, L. Peng, S. Adam, and

- F. Guinea, Extended magic phase in twisted graphene multilayers, *Physical Review Research* **6**, 013165 (2024).
- [36] F. K. Popov and G. Tarnopolsky, Magic angle butterfly in twisted trilayer graphene, *Physical Review Research* **5**, 043079 (2023).
- [37] A. Banerjee, Z. Hao, M. Kreidel, P. Ledwith, I. Phinney, J. M. Park, A. Zimmerman, M. E. Wesson, K. Watanabe, T. Taniguchi, *et al.*, Superfluid stiffness of twisted trilayer graphene superconductors, *Nature* **638**, 93 (2025).
- [38] M. Tanaka, J. Í.-j. Wang, T. H. Dinh, D. Rodan-Legrain, S. Zaman, M. Hays, A. Almanakly, B. Kannan, D. K. Kim, B. M. Niedzielski, *et al.*, Superfluid stiffness of magic-angle twisted bilayer graphene, *Nature* **638**, 99 (2025).
- [39] Y. Xie, A. T. Pierce, J. M. Park, D. E. Parker, J. Wang, P. Ledwith, Z. Cai, K. Watanabe, T. Taniguchi, E. Khalaf, *et al.*, Strong interactions and isospin symmetry breaking in a supermoiré lattice, *Science*, ead12544 (2025).
- [40] S. Turkel, J. Swann, Z. Zhu, M. Christos, K. Watanabe, T. Taniguchi, S. Sachdev, M. S. Scheurer, E. Kaxiras, C. R. Dean, *et al.*, Orderly disorder in magic-angle twisted trilayer graphene, *Science* **376**, 193 (2022).
- [41] H. Kim, Y. Choi, C. Lewandowski, A. Thomson, Y. Zhang, R. Polski, K. Watanabe, T. Taniguchi, J. Alicea, and S. Nadj-Perge, Evidence for unconventional superconductivity in twisted trilayer graphene, *Nature* **606**, 494 (2022).
- [42] H. Kim, Y. Choi, É. Lantagne-Hurtubise, C. Lewandowski, A. Thomson, L. Kong, H. Zhou, E. Baum, Y. Zhang, L. Holleis, *et al.*, Imaging intervalley coherent order in magic-angle twisted trilayer graphene, *Nature* **623**, 942 (2023).
- [43] C. Shen, P. J. Ledwith, K. Watanabe, T. Taniguchi, E. Khalaf, A. Vishwanath, and D. K. Efetov, Dirac spectroscopy of strongly correlated phases in twisted trilayer graphene, *Nature Materials* **22**, 316 (2023).
- [44] J. C. Hoke, Y. Li, J. May-Mann, K. Watanabe, T. Taniguchi, B. Bradlyn, T. L. Hughes, and B. E. Feldman, Uncovering the spin ordering in magic-angle graphene via edge state equilibration, *Nature communications* **15**, 4321 (2024).
- [45] L.-Q. Xia, S. C. de la Barrera, A. Uri, A. Sharpe, Y. H. Kwan, Z. Zhu, K. Watanabe, T. Taniguchi, D. Goldhaber-Gordon, L. Fu, *et al.*, Topological bands and correlated states in helical trilayer graphene, *Nature Physics* **21**, 239 (2025).
- [46] J. C. Hoke, Y. Li, Y. Hu, J. May-Mann, K. Watanabe, T. Taniguchi, T. Devakul, and B. E. Feldman, Imaging supermoiré relaxation and conductive domain walls in helical trilayer graphene, *arXiv preprint arXiv:2410.16269* (2024).
- [47] A. L. Sharpe, E. J. Fox, A. W. Barnard, J. Finney, K. Watanabe, T. Taniguchi, M. Kastner, and D. Goldhaber-Gordon, Emergent ferromagnetism near three-quarters filling in twisted bilayer graphene, *Science* **365**, 605 (2019).
- [48] Y. Choi, H. Kim, C. Lewandowski, Y. Peng, A. Thomson, R. Polski, Y. Zhang, K. Watanabe, T. Taniguchi, J. Alicea, *et al.*, Interaction-driven band flattening and correlated phases in twisted bilayer graphene, *Nature Physics* **17**, 1375 (2021).
- [49] J. Xiao, A. Inbar, J. Birkbeck, N. Gershon, Y. Zamir, T. Taniguchi, K. Watanabe, E. Berg, and S. Ilani, The interacting energy bands of magic angle twisted bilayer graphene revealed by the quantum twisting microscope, *arXiv preprint arXiv:2506.20738* (2025).
- [50] Q. Hu, S. Liang, X. Li, H. Shi, X. Dai, and Y. Xu, Link between cascade transitions and correlated chern insulators in magic-angle twisted bilayer graphene, *arXiv preprint arXiv:2406.08734* (2024).
- [51] Z. Zhang, S. Wu, D. Călugăru, H. Hu, T. Taniguchi, K. Watanabe, A. B. Bernevig, and E. Y. Andrei, Heavy fermions, mass renormalization and local moments in magic-angle twisted bilayer graphene via planar tunneling spectroscopy, *arXiv preprint arXiv:2503.17875* (2025).
- [52] Z.-D. Song and B. A. Bernevig, Magic-angle twisted bilayer graphene as a topological heavy fermion problem, *Physical review letters* **129**, 047601 (2022).
- [53] F. Steglich and S. Wirth, Foundations of heavy-fermion superconductivity: lattice kondo effect and mott physics, *Reports on Progress in Physics* **79**, 084502 (2016).
- [54] M. Tinkham, *Introduction to superconductivity* (Courier Corporation, 2004).
- [55] J. Yu, M. Xie, B. A. Bernevig, and S. Das Sarma, Magic-angle twisted symmetric trilayer graphene as a topological heavy-fermion problem, *Physical Review B* **108**, 035129 (2023).
- [56] Y. H. Kwan, G. Wagner, T. Soejima, M. P. Zaletel, S. H. Simon, S. A. Parameswaran, and N. Bultinck, Kekulé spiral order at all nonzero integer fillings in twisted bilayer graphene, *Physical Review X* **11**, 041063 (2021).
- [57] G. Wagner, Y. H. Kwan, N. Bultinck, S. H. Simon, and S. Parameswaran, Global phase diagram of the normal state of twisted bilayer graphene, *Physical review letters* **128**, 156401 (2022).
- [58] S. Liu, E. Khalaf, J. Y. Lee, and A. Vishwanath, Nematic topological semimetal and insulator in magic-angle bilayer graphene at charge neutrality, *Physical Review Research* **3**, 013033 (2021).
- [59] D. E. Parker, T. Soejima, J. Hauschild, M. P. Zaletel, and N. Bultinck, Strain-induced quantum phase transitions in magic-angle graphene, *Physical review letters* **127**, 027601 (2021).
- [60] Z. Bi, N. F. Yuan, and L. Fu, Designing flat bands by strain, *Physical Review B* **100**, 035448 (2019).
- [61] L.-Q. Xia, A. Uri, J. Yan, A. Sharpe, F. Gaggioli, N. S. Ticea, J. May-Mann, K. Watanabe, T. Taniguchi, L. Fu, *et al.*, Magic continuum in multi-moiré twisted trilayer graphene, *arXiv preprint arXiv:2509.03583* (2025).
- [62] B. Amorim and E. V. Castro, Electronic spectral properties of incommensurate twisted trilayer graphene, *arXiv preprint arXiv:1807.11909* (2018).
- [63] M. Koshino, Interlayer interaction in general incommensurate atomic layers, *New Journal of Physics* **17**, 015014 (2015).
- [64] L. Wang, I. Meric, P. Huang, Q. Gao, Y. Gao, H. Tran, T. Taniguchi, K. Watanabe, L. Campos, D. Muller, *et al.*, One-dimensional electrical contact to a two-dimensional material, *Science* **342**, 614 (2013).
- [65] J. Pizarro, M. Rösner, R. Thomale, R. Valentí, and T. Wehling, Internal screening and dielectric engineering in magic-angle twisted bilayer graphene, *Physical Review B* **100**, 161102 (2019).

METHODS

Spectral function calculations

In this section, we describe our method for calculating the electronic structure at incommensurate twist angles. We use the method described in Ref. [29] (see also Refs. [33, 62, 63]), which we briefly review here. An eigenstate is expressed as

$$|\psi_{\mathbf{k},n}\rangle = \sum_{\mathbf{G}_2, \mathbf{G}_3, \alpha} \phi_{1,\mathbf{k},\alpha}^{(n)} |1, \mathbf{k} + \mathbf{G}_2 + \mathbf{G}_3, \alpha\rangle + \sum_{\mathbf{G}_1, \mathbf{G}_3, \alpha} \phi_{2,\mathbf{k},\alpha}^{(n)} |2, \mathbf{k} + \mathbf{G}_1 + \mathbf{G}_3, \alpha\rangle + \sum_{\mathbf{G}_1, \mathbf{G}_2, \alpha} \phi_{3,\mathbf{k},\alpha}^{(n)} |3, \mathbf{k} + \mathbf{G}_1 + \mathbf{G}_2, \alpha\rangle \quad (1)$$

where $|\ell, \mathbf{k}, \alpha\rangle$ is the graphene Bloch state on layer ℓ at momentum \mathbf{k} (defined modulo \mathbf{G}_ℓ), n is the eigenstate index, $\alpha = A, B$ is the sublattice (spin degeneracy is assumed throughout), \mathbf{G}_ℓ is the atomic reciprocal lattice vectors for layer ℓ . Relative to an unrotated graphene reciprocal lattice vector \mathbf{G}_0 , $\mathbf{G}_\ell = \mathbf{R}(\theta_\ell)\mathbf{G}_0$, where θ_ℓ is the twist angle of layer ℓ .

The $\phi_{\ell,\mathbf{k},\alpha}^{(n)}$ are complex wavefunction coefficients obtained by diagonalizing the Hamiltonian matrix, which consists of an intralayer and interlayer part. For the intralayer part, we take the Dirac dispersion. The non-zero matrix elements are given by

$$\langle \ell, \mathbf{k}, \alpha | H_\ell | \ell, \mathbf{k}, \alpha' \rangle = v_F \begin{pmatrix} 0 & (k_x - ik_y - [K_{\ell,x} - iK_{\ell,y}])e^{i\theta_\ell} \\ \text{c.c.} & 0 \end{pmatrix}_{\alpha\alpha'} \quad (2)$$

where \mathbf{K}_ℓ is the graphene K -points of layer ℓ .

The interlayer tunneling term is given by

$$\langle \ell, \mathbf{k} + \mathbf{G}_{123}, \alpha | H_{\ell\ell'} | \ell', \mathbf{k} + \mathbf{G}_{123}, \alpha' \rangle = t(\mathbf{k} + \mathbf{G}_{123}) e^{i\mathbf{G}_\ell \cdot \boldsymbol{\tau}_\alpha^\ell - i\mathbf{G}_{\ell'} \cdot \boldsymbol{\tau}_{\alpha'}^{\ell'}} \begin{pmatrix} \kappa & 1 \\ 1 & \kappa \end{pmatrix}_{\alpha\alpha'} \quad (3)$$

where $\mathbf{G}_{123} \equiv \mathbf{G}_1 + \mathbf{G}_2 + \mathbf{G}_3$ is the sum of any three reciprocal lattice vectors, and $\boldsymbol{\tau}_\alpha^\ell$ are the positions of the sublattice α atoms in the graphene unit cell of layer ℓ , and κ is the chiral ratio suppressing AA and BB tunneling. In this expression, we have used the momentum space periodicity $|\ell, \mathbf{k} + \mathbf{G}_\ell, \alpha\rangle \equiv |\ell, \mathbf{k}, \alpha\rangle$.

For a given \mathbf{k} , the Hamiltonian matrix is constructed by considering all \mathbf{G}_{123} up to a cutoff $|\mathbf{G}_\ell| < 7.1K$. We take a linear approximation to the tunneling amplitude, $t(\mathbf{k}) \approx t_0 + t_1(|\mathbf{k}| - K)$, where K is the magnitude of the K point momentum, for $0 < |\mathbf{k}| < 1.4K$ and zero

otherwise — for our choice of cutoff, this is equivalent to the first harmonic approximation of the Bistritzer-MacDonald model. The matrix is then diagonalized to obtain the list of eigenenergies $\varepsilon_{n\mathbf{k}}$ and eigenvectors $\phi_{\ell,\mathbf{k},\alpha}^{(n)}$. The layer-resolved spectral weight is obtained by $w_{n\mathbf{k}\ell} = \sum_\alpha |\phi_{\ell,\mathbf{k},\alpha}^{(n)}(\mathbf{0}, \mathbf{0})|^2$. In the spectral functions shown in Fig. 1 and Fig. ED1, the energy $\varepsilon_{n\mathbf{k}}$ is plotted along a path in \mathbf{k} , with the width of the line proportional to the total spectral weight $\sum_\ell w_{n\mathbf{k}\ell}$ and the color indicating the direction of the vector $(w_{n\mathbf{k}1}, w_{n\mathbf{k}2}, w_{n\mathbf{k}3})$ as indicated in the color triangle. The parameters used are $v_F = 0.88 \times 10^6$ m/s, $t_0 = 0.11$ eV, $t_1 = -0.227$ eVÅ, and $\kappa = 0.7$.

Device fabrication

The TTG heterostructure studied was fabricated using standard dry transfer techniques with poly (bisphenol A carbonate)/polydimethylsiloxane (PC/PDMS) transfer slides. A monolayer graphene flake was cut into 3 pieces with a conductive atomic force microscope (AFM) tip in contact mode. An exfoliated hBN flake (42 nm thick) was then used to sequentially pick up each section at the desired twist angle before placing it on top of a prefabricated stack of few-layer graphite and hBN (33 nm thick), which had been previously vacuum annealed at 400° C for 8 hours to ensure cleanliness of the surface. The full stack was then patterned with standard electron beam lithography techniques followed by etching and metallization to form edge contacts [64] (Fig. ED6d). After measurements in the SET microscope, the device was further patterned with a Cr/Au top metallic gate, etched into a Hall bar geometry, and patterned with additional edge contacts (Fig. ED6e-f).

We note that although the addition of a metallic top gate introduces a potential new screening layer to the sample, the top gate sits atop a $d = 42$ nm thick hBN dielectric layer, which is significantly greater than the $\lambda_{12} \sim 10 - 15$ nm moiré wavelength associated with layers 1 and 2. Thus we expect the top gate to have negligible effects related to Coulomb screening, which only becomes significant when $d < \lambda_{12}$ [17, 18, 65].

Scanning SET measurements

The SET tip was fabricated by evaporating aluminum onto a pulled quartz rod and has an estimated diameter of 100 nm at its apex. The tip is brought near the sample surface and scanning SET measurements were performed in a Unisoku USM 1300 scanning probe microscope with a microscope head customized for scanning SET operation. A 5 mV a.c. excitation at 823 Hz was applied to the sample, while a 20 mV a.c. excitation at 911.7 Hz was applied to the back gate. We then measure the inverse compressibility $d\mu/dn \propto I_{BG}/I_{2D}$, where I_{BG} and I_{2D}

are the measured SET current demodulated at the back gate and sample frequencies, respectively, using standard lock-in techniques. A d.c. offset voltage V_{2D} is applied to the sample to maintain maximum sensitivity of the SET and minimize tip-induced doping. SET measurements were taken at $T = 1.6$ K or 330 mK, as specified in the figure captions.

Transport measurements

Transport measurements were performed in a Leiden Cryogenics CF-900 dilution refrigerator using a custom probe. The measurement lines are equipped with electronic filtering thermally anchored at the mixing chamber stage to obtain a low electron temperature and reduce high-frequency noise. There are two stages of filtering. First, the wires are passed through a cured mixture of epoxy and bronze powder to filter GHz frequencies. Subsequently, low-pass RC filters mounted on sapphire plates attenuate MHz frequencies. Samples were mounted using a Kyocera custom 32-contact ceramic leadless chip carrier (drawing PB-44567-Mod with no nickel sticking layer under gold, to reduce spurious magnetic effects). Stanford Research Systems SR830 lock-in amplifiers with NF Corporation LI-75A voltage preamplifiers were used to perform four-terminal resistance measurements. A 1 G Ω bias resistor was used to apply an a.c. bias current of up to 5 nA RMS at low frequencies. Keithley 2400 source-measure units were used to apply voltages to the gates.

Determination of θ_{12}

The conversion from applied voltages to carrier density n in the SET experiment is determined by the geometric capacitance between the graphite bottom gate and the TTG sample: $n = C_b(V_b - V_{2D})/e$, where $V_b - V_{2D}$ is the difference in the voltages applied to the bottom gate and the sample, and e is the electron charge. The capacitance C_b between the bottom gate and sample is determined from the slopes of quantum Hall features emanating from charge neutrality in Landau fan measurements, which are quantized according to fundamental constants. This extracted capacitance is consistent with a parallel plate capacitor where the separation between plates is equal to the hBN thickness measured by atomic force microscopy.

In transport measurements, the dual gated geometry of the device allows for independent control of n and the perpendicular electric displacement field D , where $n = C_t V_t/e + C_b V_b/e$ and $D = (C_t V_t/e - C_b V_b/e)/(2\epsilon_0)$. Here, V_b (V_t) is the voltage applied to the bottom (top) gate, C_b (C_t) is the bottom (top) gate capacitance, and ϵ_0 is the vacuum permittivity. The capacitance C_b (C_t) between the bottom (top) gate and sample is again determined from the slopes of quantum Hall features emanating from charge neutrality in Landau fan measurements, which are quantized according to fundamental constants.

The extracted C_b from transport experiments match with the extracted C_b from SET experiments.

In both SET and transport measurements, the superlattice carrier density n_s , associated with the twist angle between layers 1 and 2, is determined by fitting the $\nu = \pm 4$ states in a finite magnetic field B to the Str da formula $\frac{\partial n}{\partial B} = \pm 2 \frac{e}{h}$, where the ± 2 comes from the filling of the Dirac-like Landau levels, and extrapolating to $B = 0$. In scanning SET measurements at $B = 0$, we instead take n_s to be $n_s = (n(\nu = 4) - n(\nu = -4))/2$, where $n(\nu = \pm 4)$ is the carrier density of the peak of the $\nu = \pm 4$ incompressible states. The interlayer twist angle θ_{12} is then found by $n_s = 4/A \approx 8\theta_{12}^2/\sqrt{3}a^2$. Here, A is the moir  lattice unit cell area associated with the moir  superlattice of layers 1 and 2, and $a = 0.246$ nm is the graphene lattice constant. We find empirically that the two methods to determine θ_{12} give results with negligible differences.

Hofstadter spectrum measurement

The procedure to measure the correlated Hofstadter spectrum from inverse compressibility experiments is discussed in detail in the Supplement of Ref. [13]. In short, we perform a measurement of $d\mu/dn$ as a function of n and B (Fig. ED2a). We then integrate $d\mu/dn$ across the entire density range for each magnetic field B to obtain $\mu(n, B)$. N points are evenly sampled across the density range. This discrete sampling procedure produces an energy spectrum $E(i, B)$, where $i \in [1, 2, \dots, N]$. Plotting $E(i, B)$ for each B produces the Hofstadter spectrum in Fig. ED2c.

Estimation of θ_{23}

Nominally, the twist angle θ_{23} between layers 2 and 3 also creates a moir  superlattice. However, due to the relatively large θ_{23} , any features related to the filling of this secondary moir  superlattice are inaccessible within the experimentally available gate voltage range, making it challenging to unambiguously and precisely determine θ_{23} experimentally. However, we can estimate θ_{23} by measuring the renormalized Fermi velocity v_F^* of the Dirac cone associated with layer 3.

Ignoring tunneling between layers 1 and 3, and assuming both the interlayer AA/BB and AB/BA hopping elements are equal to t_0 , the renormalized Fermi velocity of layer 3, is given by

$$v_F^* = \frac{1 - 3\alpha_{23}^2 v_F^0}{1 + 6\alpha_{23}^2 v_F^0}, \quad (4)$$

where $\alpha_{23} = t_0/(\hbar v_F^0 k_{\theta_{23}})$ and $k_{\theta} = 8\pi \sin(\theta/2)/(3a)$ [29, 33]. This gives a direct relation between θ_{23} and v_F^* :

$$\sin(\theta_{23}/2) = \frac{3t_0 a}{8\pi \hbar v_F^0} \sqrt{\frac{3(1 + 2v_F^*/v_F^0)}{1 - v_F^*/v_F^0}}. \quad (5)$$

We set $t_0 = 0.105$ eV and $v_F^0 = 1 \times 10^6$ m/s, consistent with previous experimentally estimated values [29]. The above equation allows us to estimate θ_{23} by experimentally measuring v_F^* . The relationship between θ_{23} and v_F^* is plotted in Fig. ED2d.

At higher energies, the experimentally measured Hofstadter spectrum displays a set of dispersing features with enhanced density of states (DOS), which we identify as the Landau levels (LLs) of the Dirac cone in a finite magnetic field B (Fig. ED2b). We fit these states to the standard \sqrt{B} field dependence of Dirac Landau levels:

$$E = E_0 + \text{sgn}(N)v_F^*\sqrt{2e\hbar NB}, \quad (6)$$

where N , e and \hbar are the LL index, electron charge and reduced Planck constant, respectively, and E_0 and v_F^* are left as fitting parameters. We specifically fit to the most prominent observed LLs ($N = \pm 1$, and ± 2) to estimate v_F^* . From this procedure we find $v_F^* = 0.81 \times 10^6$ m/s, corresponding to $\theta_{23} \approx 3.45^\circ$. This is consistent with the estimation of $\theta_{23} \sim 3\text{--}4^\circ$ from the relative twist angles between the flat edges of layers 2 and 3 seen in optical images during sample fabrication Fig. ED6. Lastly, we note that although the set up of our SET experiment necessarily introduces a small displacement field D that cannot be independently controlled, the effect of this displacement field is negligible and does not meaningfully impact the extracted v_F^* [30].

Extraction of thermodynamic gaps

The thermodynamic gap of an incompressible state is given by the corresponding step in the chemical potential Δ , which is obtained by integrating the inverse compressibility $d\mu/dn$:

$$\Delta = \mu(n_+) - \mu(n_-) = \int_{n_-}^{n_+} \left(\frac{d\mu}{dn} - \kappa_B^{-1} \right) dn, \quad (7)$$

where $n_{+(-)}$ is the upper (lower) bound in density of the gapped state and κ_B^{-1} is a small constant background that may need to be subtracted. We followed the same procedure as is described in detail in Ref. [13].

Extraction of sawtooth compressibility strength

The strength of the sawtooth in compressibility for the conduction (valence) band $\sigma_{e(h)}$ is calculated by the standard deviation of $d\mu/dn$ between $0.5 < \nu < 3.5$ ($-3.5 < \nu < -0.5$). Before calculating the standard deviation, a Savitzky-Golay filter is applied to the data to: 1) remove contributions from noise in the measurement and 2) remove contributions of the peak at $\nu = \pm 2$ to the extracted standard deviation, thereby isolating only contributions related to the sawtooth compressibility itself. We find that the application of the Savitzky-Golay filter

has no impact on the position or width of the peak in $\sigma_{e(h)}$ and simply shifts $\sigma_{e(h)}$ down by an overall constant (Fig. ED4).

Further discussion of $1 \times 1 \mu\text{m}^2$ spatial map

Fig. ED5 shows the systemic spatial dependence of $\Delta\mu_f = \Delta\mu_e + \Delta\mu_h$, Δ_2 , and $\sigma_{e(h)}$ in a $1 \times 1 \mu\text{m}^2$ area of the sample ($\Delta_{-2} = 0$ throughout the entire area). θ_{12} is the primary driver of the observed correlation physics. However, even at constant θ_{12} , systematic spatial variability in each signature is evident, as seen Fig. ED5h-k, where the color of each data point represent its x -coordinate in the grid. From these spatially-resolved measurements, we find that for a given θ_{12} both $\Delta\mu_f$ and Δ_2 are suppressed from left (blue) to right (red), while σ_e is instead enhanced. This highlights that the detailed microscopic conditions (beyond just θ_{12}) that favor Δ_2 or σ_e differ.

The specific microscopic origins of the 2D spatial dependence in Fig. ED5 is difficult to determine unambiguously from our experiment. More extensive theoretical modeling is needed to understand it fully, but that is beyond the scope of this work. We discuss two possible origins of the spatial variability observed in Fig. ED5 even for constant θ_{12} : local variations in strain, or changes in θ_{23} . We speculate that the latter are the more likely explanation of the data than variations in strain, as we discuss further below.

In MATBG, increased strain is predicted to enhance $\Delta\mu_f$, but suppress Δ_2 [8]. Due to the relatively weak coupling between layers 2 and 3, a similar trend may be expected for this TTG device (though we are not aware of theoretical modeling for generic twist angles in TTG). In contrast to this expectation from strain, we instead observe the opposite trend: for constant θ_{12} , we find in Fig. ED5h-i that both $\Delta\mu_f$ and Δ_2 generally decrease and increase together in space. Additionally, Fig. ED1 shows that for constant θ_{12} , increasing θ_{23} within the range of θ_{23} expected in our experiment tends to flatten the (single particle) bands further. Thus, although small spatial variability in strain is likely present, it is reasonable that variations in θ_{23} may be the dominant contributor to the observed spatial trends in Fig. ED5.

Extraction of the superconducting critical temperature

In transport experiments in two-dimensional systems, three criteria are required to conclusively determine the presence of superconductivity: 1) zero longitudinal resistance R_{xx} , 2) non-linear d.c. I - V characteristics with zero voltage drop up to a critical current I_c , and 3) oscillations in the critical current as a function of perpendicular magnetic field that indicate phase-coherent transport. Our sample meets all three criteria (Fig. 3d-f), but verifying

all three criteria at every (n, D) point where superconductivity appears is impractical.

To characterize superconductivity at every (n, D) point, we measure R_{xx} maps as a function of n and D , and then vary the temperature T in small, discrete steps. From this three-dimensional data set, we can extract the critical temperature T_c as a function of n and D (Fig. 3g-j). We ascribe a finite T_c only to data points where R_{xx} displays the characteristic superconducting $R_{xx}-T$ transition curve (Fig. 3d, for example) and where R_{xx} falls below $100\ \Omega$. If any (n, D) point does not meet both of these criteria we assign $T_c = 0$ —either the sample is not superconducting at the specific (n, D) , or the superconductivity does not fully develop at base temperature. To determine T_c , we first linearly fit the $R_{xx}-T$ curves at high T , above the onset of the superconducting transition, and extrapolate to $T = 0$. We define this to be the normal-state resistance $R_{xx}^n(T)$ as a function of T . We then take T_c to be the temperature where 10% of the extrapolated normal-state $R_{xx}^n(T)$ line intersects the measured $R_{xx}-T$ curve.

Lastly, while we plot the optimal (maximal) T_c in Fig. 4 from the n - D maps in Fig. 3g-j, we note that the qualitative shape and θ_{12} dependence of T_c is remains consistent independent of the details used to extract T_c or T_c^{opt} . This includes if we, for example, define T_c to be where R_{xx} reaches 20% of the normal state resistance (as opposed to 10%) or if we only consider superconductivity along a line cut with $V_t = 0$, which most closely approximates the conditions of SET measurements (Fig. ED8).

DATA AVAILABILITY

The data that supports the findings of this study are available from the corresponding authors upon reasonable request.

CODE AVAILABILITY

The codes that support the findings of this study are available from the corresponding authors upon reasonable request.

ACKNOWLEDGMENTS

We thank B. Andrei Bernevig, Xi Dai, Patrick Ledwith, Marc A. Kastner, Liqiao Xia, and Jiaojie Yan for helpful discussions. Scanning SET measurements were supported by the QSQM, an Energy Frontier Research Center funded by the U.S. Department of Energy (DOE), Office of Science, Basic Energy Sciences (BES), under Award # DE-SC0021238. Transport studies were supported by National Science Foundation (Grant no. NSF-DMR-2237050). K.W. and T.T. acknowledge support from the JSPS KAKENHI (Grant Numbers 21H05233

and 23H02052), the CREST (JPMJCR24A5), JST and World Premier International Research Center Initiative (WPI), MEXT, Japan. J.C.H. acknowledges support from the Stanford Q-FARM Quantum Science and Engineering Fellowship. A.S. was supported by the US Department of Energy, Office of Science, Basic Energy Sciences, Materials Sciences and Engineering Division, under Contract DE-AC02-76SF00515. Measurement infrastructure was funded in part by the Gordon and Betty Moore Foundation’s EPIQS initiative through grant GBMF9460. Part of this work was performed at the Stanford Nano Shared Facilities (SNSF), supported by the National Science Foundation under award ECCS-2026822.

AUTHOR CONTRIBUTIONS

J.C.H. and Y.L. fabricated the device. J.C.H. performed the scanning SET measurements. A.S., Y.L., and J.C.H. performed transport measurements. T.D. performed theoretical calculations. B.E.F supervised the project. K.W. and T.T provided hBN crystals. All authors participated in analysis and writing of the manuscript.

COMPETING INTERESTS

The authors declare no competing interest.

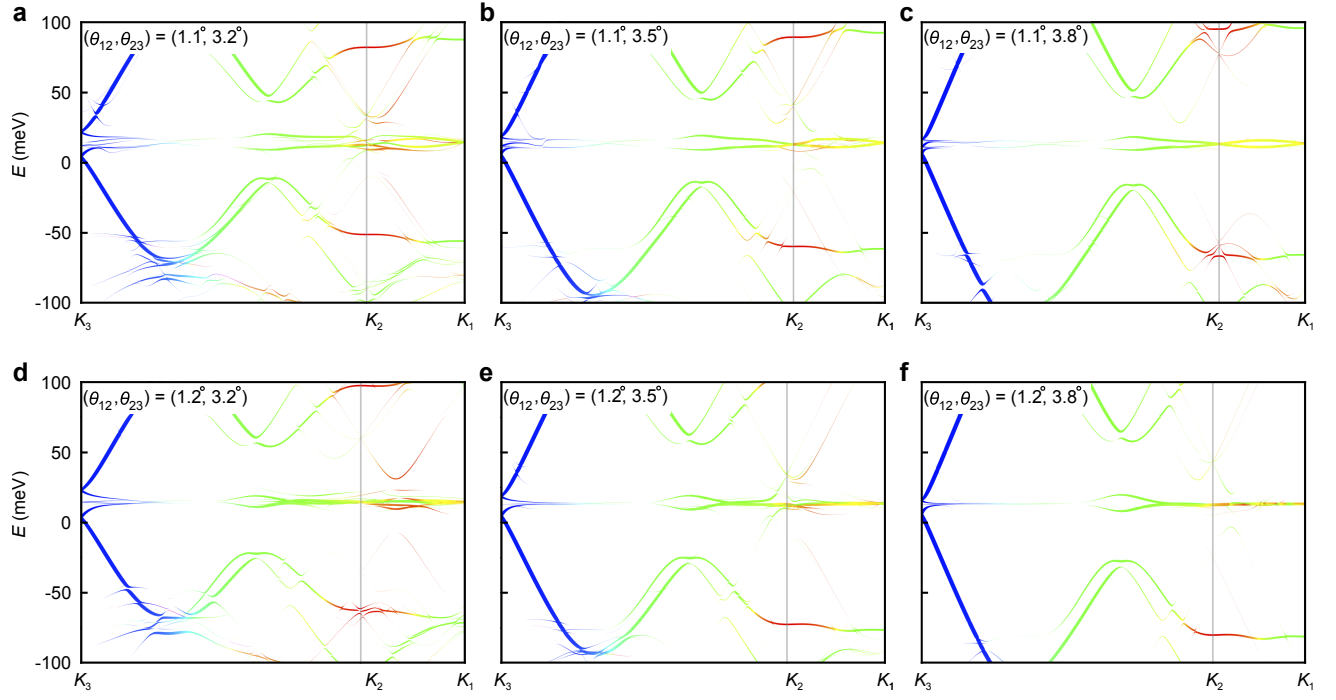


FIG. ED1. **Spectral functions of other $(\theta_{12}, \theta_{23})$ combinations.** **a-c**, Spectral function calculations for $\theta_{12} = 1.1^\circ$ and different θ_{23} along a path between the K points for each layer. **d-f**, Same as **a-c**, but for $\theta_{12} = 1.2^\circ$. Colors reflect layer character, as defined in the inset of Fig. 1b.

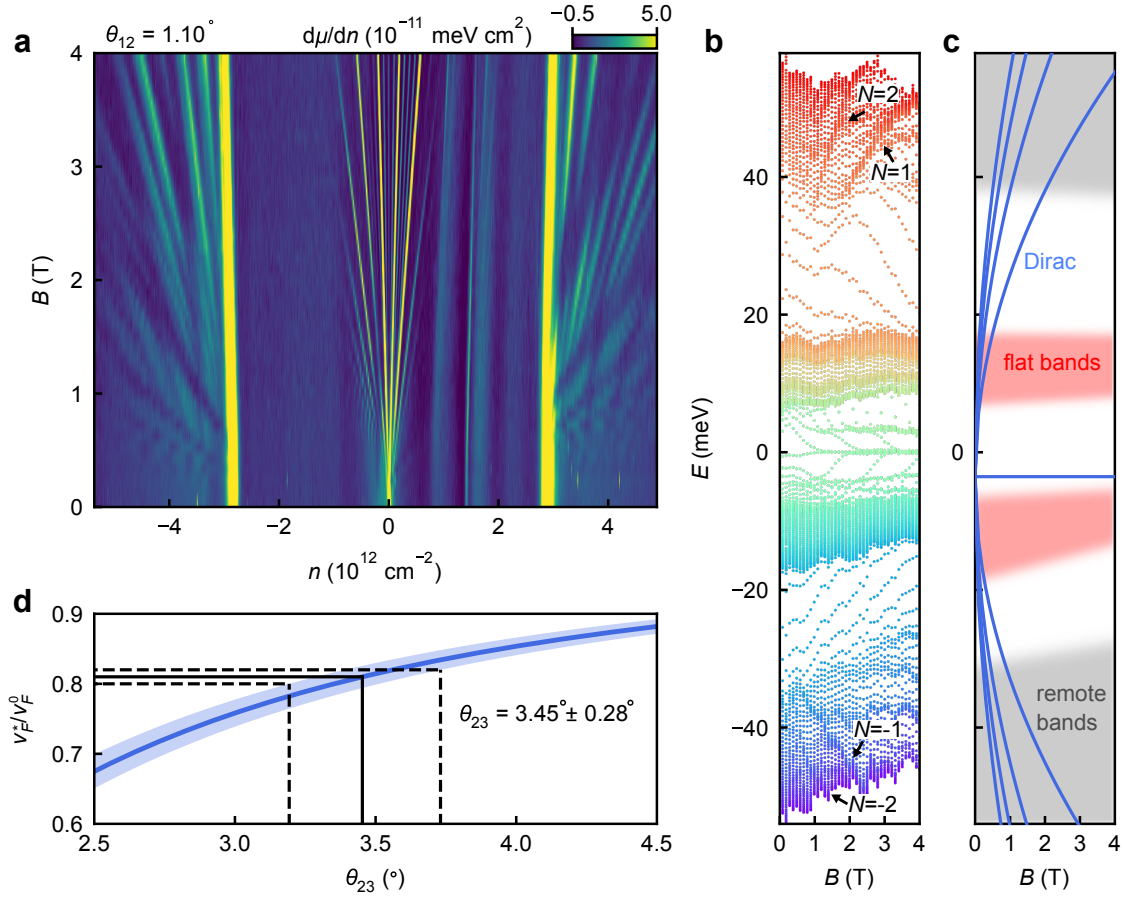


FIG. ED2. **Estimation of θ_{23} .** **a**, Landau fan measurement of $d\mu/dn$ as a function of n and B . **b**, Measurement of the many-body Hofstadter spectrum for $\theta_{12} = 1.10^\circ$, extracted from the data in **a** (Methods). The density of dots reflects the many-body density of states (DOS) and the different colors correspond to states at different n . The enhanced DOS from the $N = \pm 1, \pm 2$ LLs from the Dirac-like cone are indicated with arrows. We fit a Fermi velocity of $v_F^* = (8.1 \pm 0.1) \times 10^5 \text{ m/s}$ to the LLs from the Dirac-like cone. **c**, Schematic illustration of the origin of different features in panel **b**. **d**, Renormalized Fermi velocity v_F^* as a function of θ_{23} . The horizontal black line corresponds to $v_F^* = 8.1 \times 10^5 \text{ m/s}$, while the horizontal dashed black lines correspond to $v_F^* = (8.1 \pm 0.1) \times 10^5 \text{ m/s}$. Assuming an uncertainty in t_0 of $t_0 = 0.105 \pm .005 \text{ eV}$ (shaded light blue area), this corresponds to a twist angle $\theta_{23} = 3.45^\circ$ (vertical black line) with an uncertainty of $\pm 0.28^\circ$ (vertical black dashed lines).

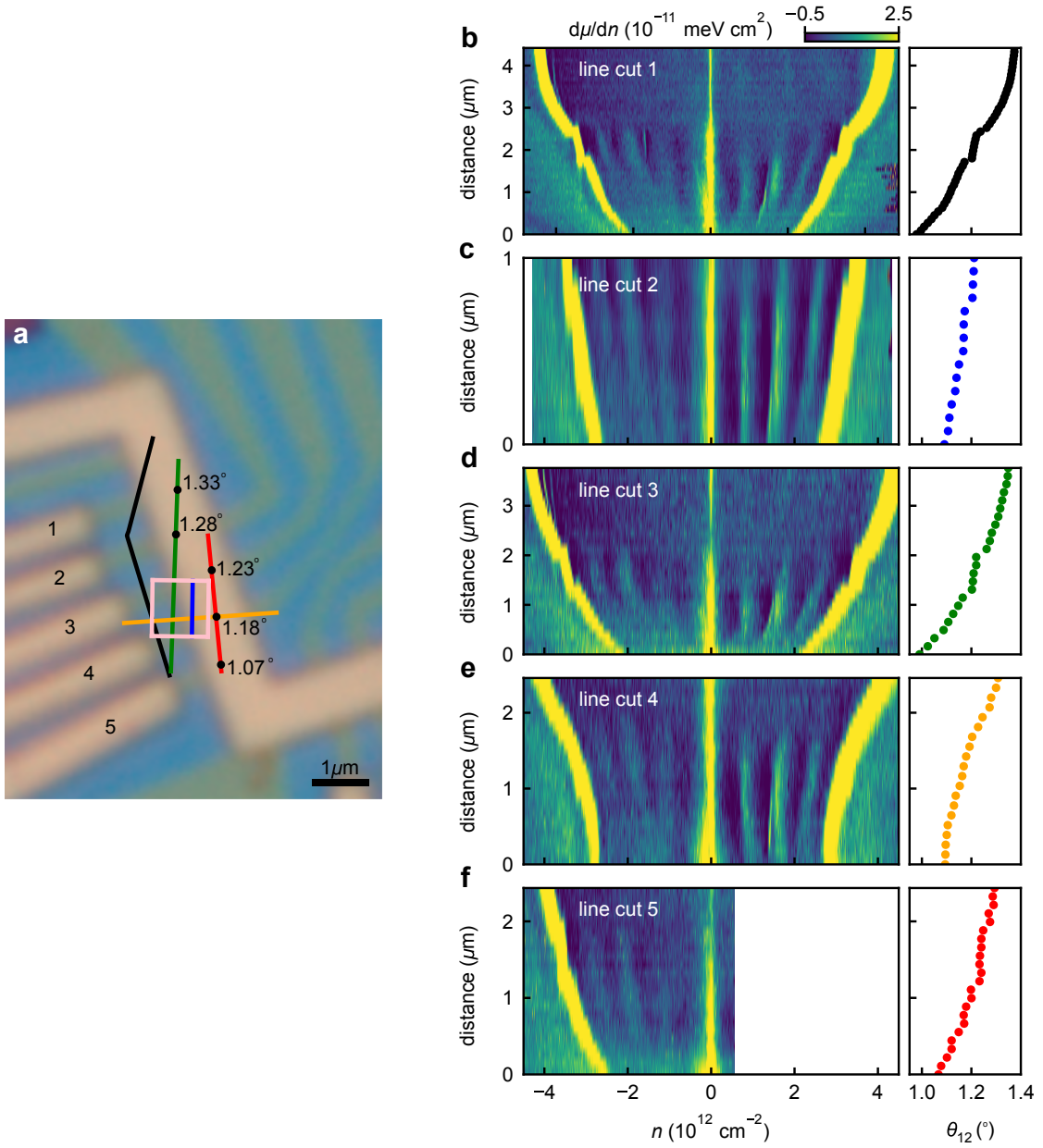


FIG. ED3. **Additional spatial line cuts of $d\mu/dn$.** **a**, Trajectories of spatial line cuts of $d\mu/dn$ overlaid on the Hall bar. The black trajectory is the line cut plotted in Fig. 2. The pink square corresponds to the location of the $1 \times 1 \mu\text{m}^2$ grid shown in Fig. ED5. **b**, $d\mu/dn$ along the black line in **a**, from bottom to top. Data are identical to those in Fig. 2a, but are reproduced for clarity and comparison. **c**, Line cut of $d\mu/dn$ along the blue line in **a**, from bottom to top. **d**, Line cut of $d\mu/dn$ along the green line in **a**, from bottom to top. **e**, Line cut of $d\mu/dn$ along the orange line in **a**, from left to right. **f**, Line cut of $d\mu/dn$ along the red line in **a**, from bottom to top. Each spatial line cut is measured at $T = 1.6 \text{ K}$.

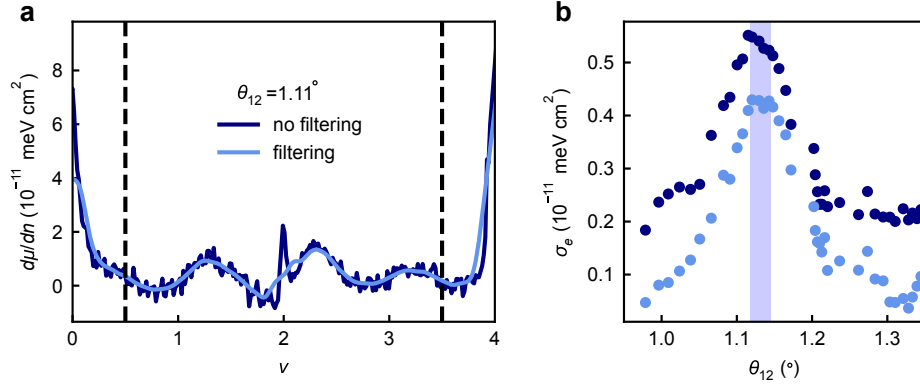


FIG. ED4. **Effect of filtering on the the strength of the sawtooth in compressibility.** **a**, Example trace of $d\mu/dn$ as a function of ν for $\theta_{12} = 1.11^\circ$ with (light blue) and without (navy) Savitzky–Golay filtering. Black dashed lines indicate the bounds between which σ_e is calculated. **b**, σ_e as a function of θ_{12} from the line cut in Fig. 2a with and without filtering. The filtered and unfiltered data sets agree qualitatively, differing only by an approximately constant vertical offset.

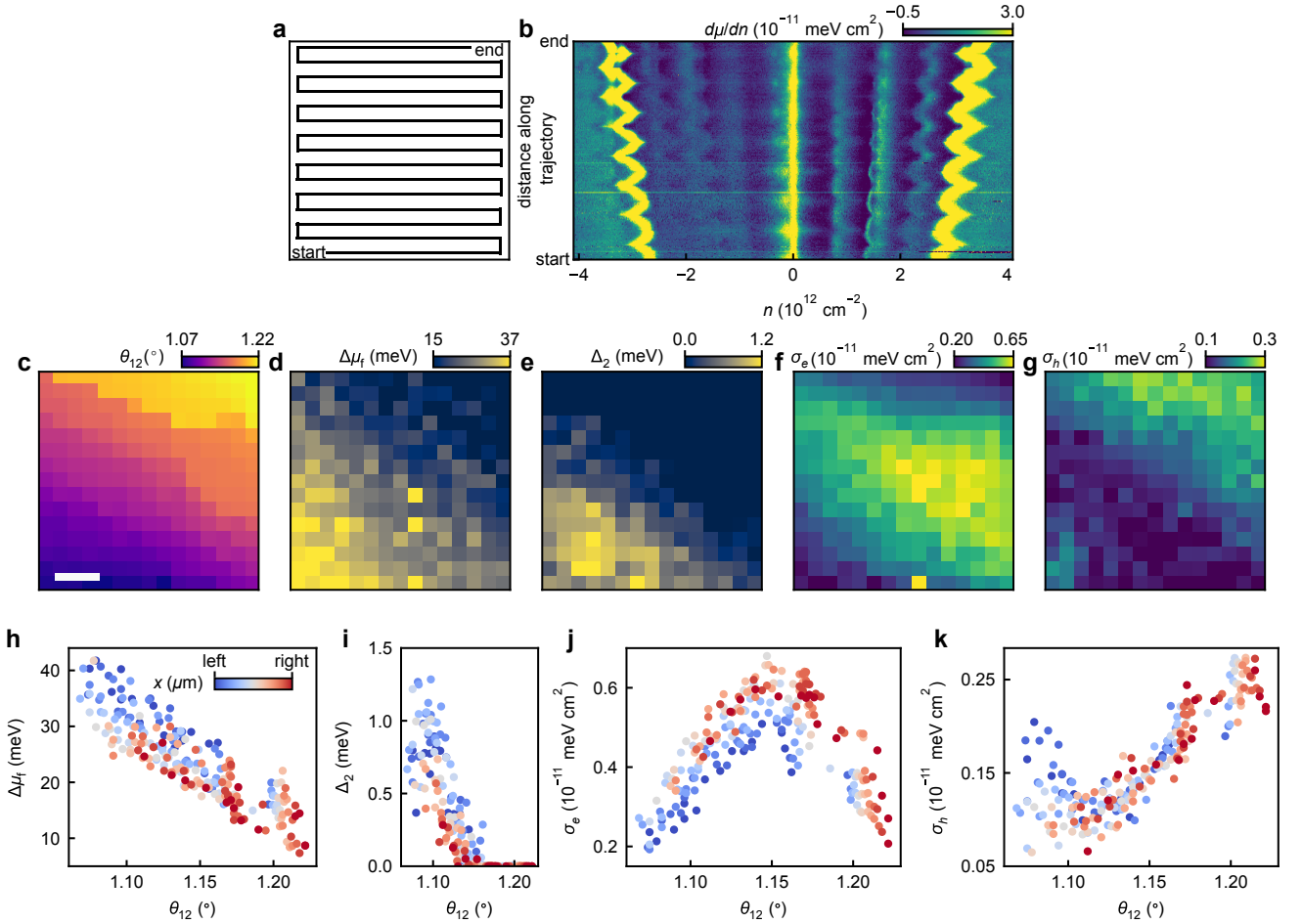


FIG. ED5. **$d\mu/dn$ within a $1 \times 1 \mu\text{m}^2$ area.** **a**, Rasterized trajectory of the SET tip during the measurement. **b**, $d\mu/dn$ as a function of n along the trajectory shown in **a**. **c–g**, Spatial map of θ_{12} , $\Delta\mu_f = \Delta\mu_e + \Delta\mu_h$, Δ_2 , σ_e , and σ_h , respectively, within the $1 \times 1 \mu\text{m}^2$ grid area. Each is extracted from the data in **b**. Note that there is no correlated state at $\nu = -2$ observed within the grid, i.e. $\Delta_{-2} = 0$ throughout this area. **h–k**, Scatter plots of $\Delta\mu_f$, Δ_2 , σ_e , and σ_h , respectively, as a function of θ_{12} . The color of each data point indicates its x -coordinate within the $1 \times 1 \mu\text{m}^2$ area.

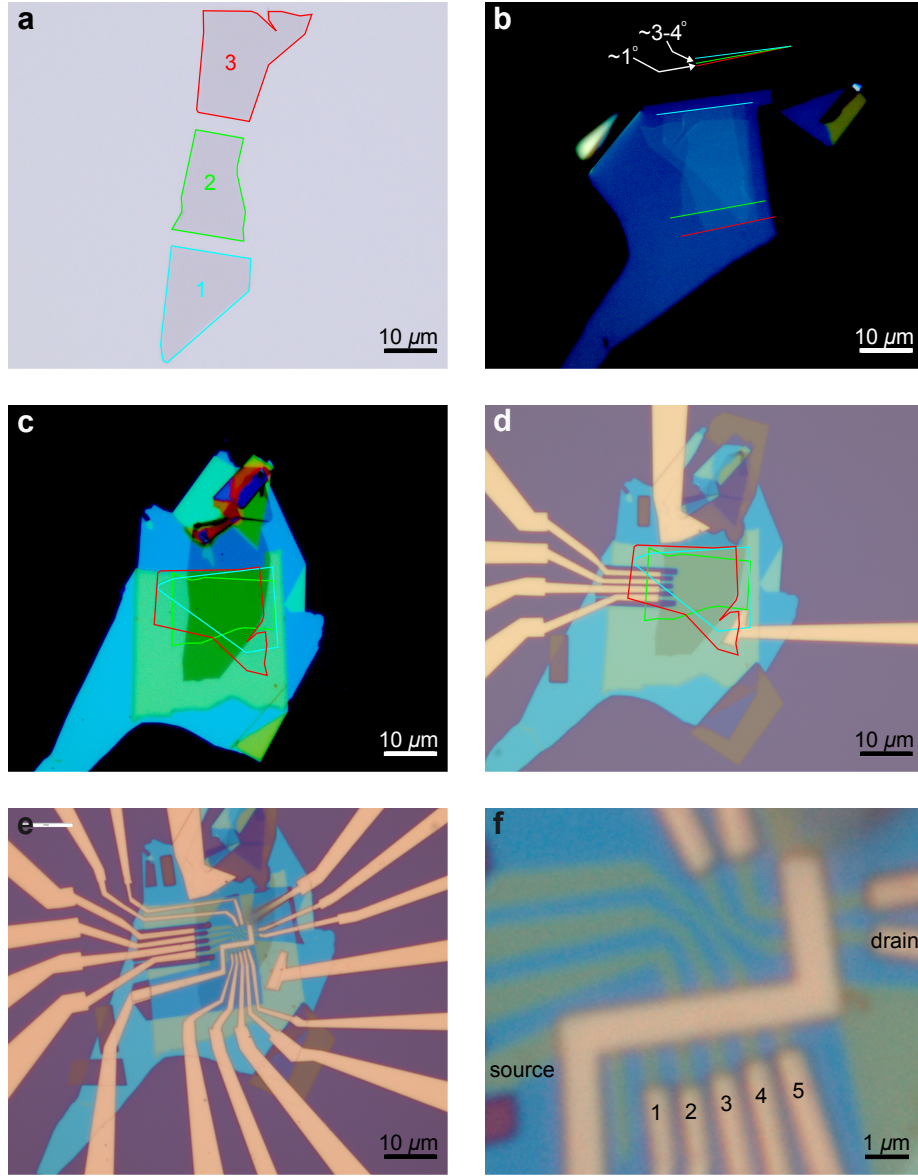


FIG. ED6. **Device fabrication.** **a**, Optical image of the graphene flakes used in the TTG device after being cut into three pieces with an atomic force microscope (AFM). **b**, The trilayer stack after being picked up with an hBN flake on the polymer stamp, but before deposition onto the bottom gate. Colored lines indicate AFM cut edges, from which we estimate $\theta_{12} \sim 1^\circ$ and $\theta_{23} \sim 3^\circ - 4^\circ$. **c**, The final stack immediately after deposition onto a pre-stacked hBN and few-layer thick graphite gate on a Si/SiO₂ substrate. **d**, Image of the device after etching and metallization, at which point it was measured with the scanning SET. **e**, Image of the device after the scanning SET experiments were completed and after additional etching and metallization into a Hall bar geometry with an added Cr/Au top gate. **f**, Zoomed in image of the Hall bar device. Contacts 1-5 were used as voltage leads for four-probe resistance measurements. The source and drain are also labeled.

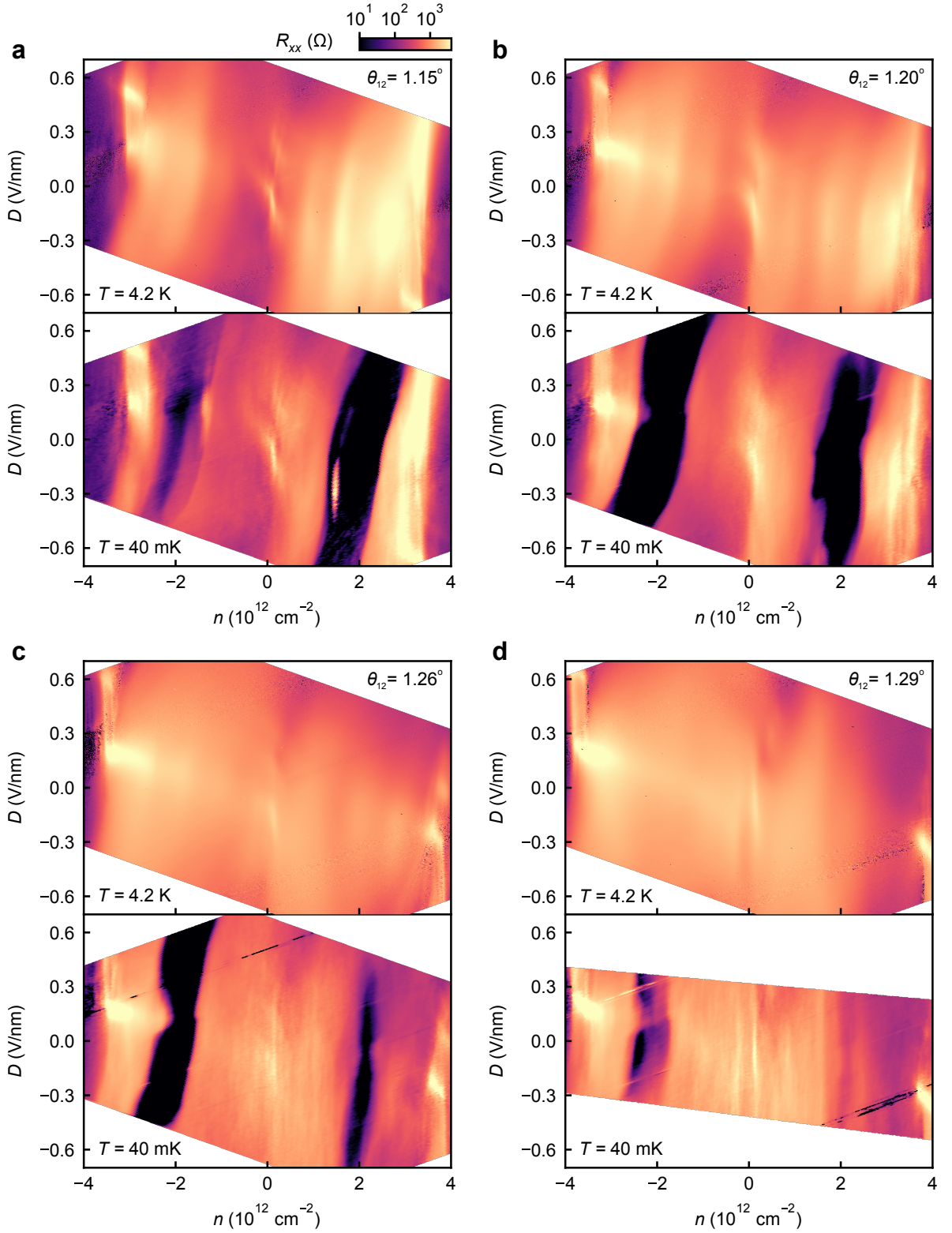


FIG. ED7. **Transport measurements at different temperatures for each contact pair.** **a**, Upper panel: longitudinal resistance R_{xx} as function of n and D for contacts 1 and 2 at $T = 4.2$ K. Lower panel: R_{xx} as a function of n and D for contacts 1 and 2 at $T = 40$ mK. **b-d**, Same as **a**, but for the other contact pairs.

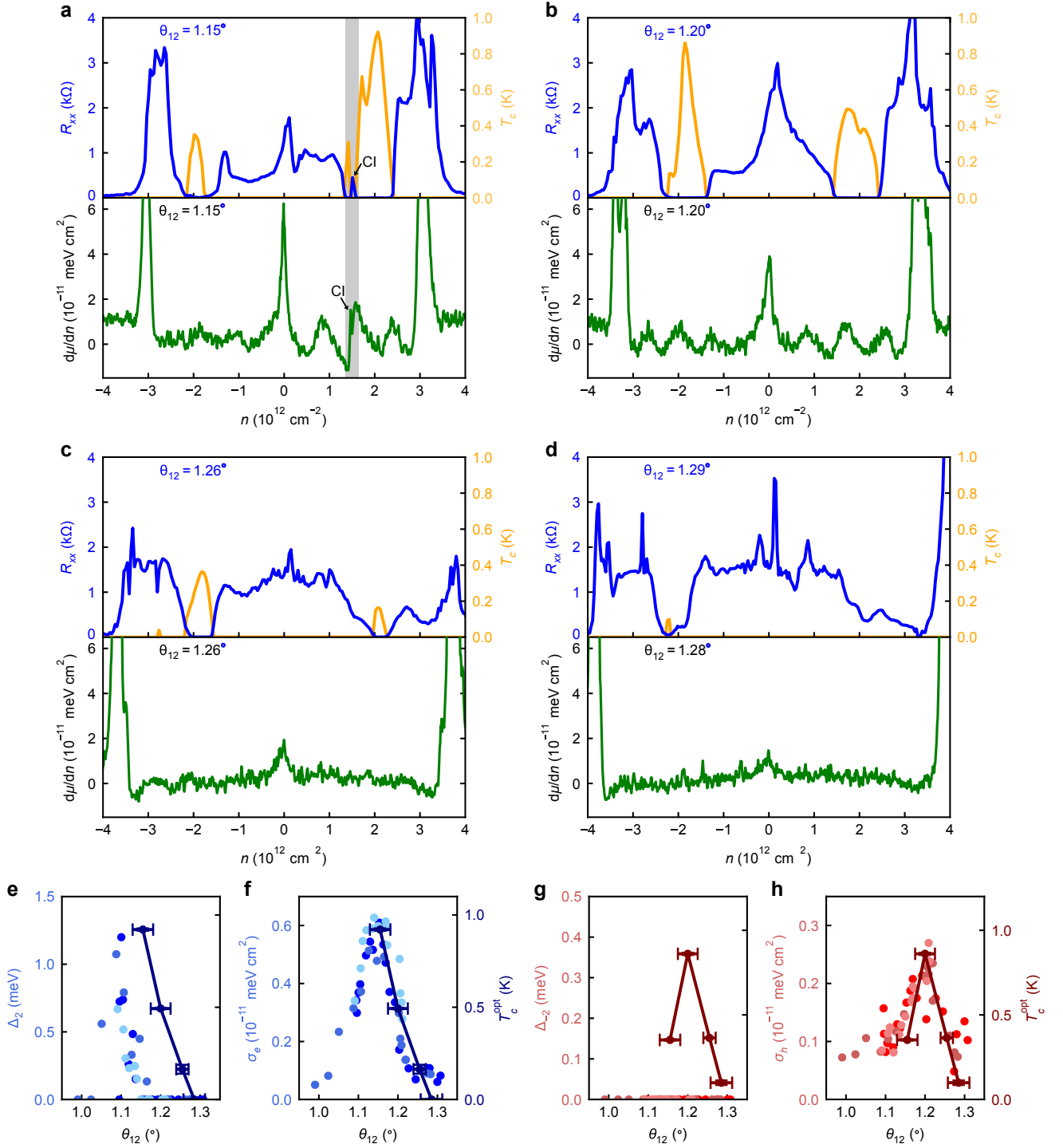


FIG. ED8. **Comparisons of electronic compressibility and transport at $V_t = 0$.** **a**, Upper panel: line traces of longitudinal resistance R_{xx} (blue) and critical temperature T_c (orange) as a function of carrier density n for the contact pair with twist angle $\theta_{12} = 1.15^\circ$. The line trace is taken with $V_t = 0$ (white dashed line in Fig. 3), which most closely approximates the conditions of SET measurements. Lower panel: line trace of the inverse compressibility $d\mu/dn$ as a function n for a spatial location along line cut 3 (Fig. ED3) where $\theta_{12} = 1.15^\circ$. A correlated insulator (CI; labeled with arrows) is seen in both the compressibility and transport measurements at this twist angle. **b-d**, Same as **a**, but for the other contact pairs. **e**, Δ_2 (left) and critical temperature at optimal doping T_c^{opt} from the $V_t = 0$ line traces for the electron-doped superconductor in **a-d** (right) as a function of θ_{12} . **f**, σ_e (left) and critical temperature at optimal doping T_c^{opt} from the $V_t = 0$ line traces for the electron-doped superconductor in **a-d** (right) as a function of θ_{12} . **g-h**, Same as **e-f**, but for hole doping. The compressibility data shown in **e-h** is the same as that shown Fig. 4.

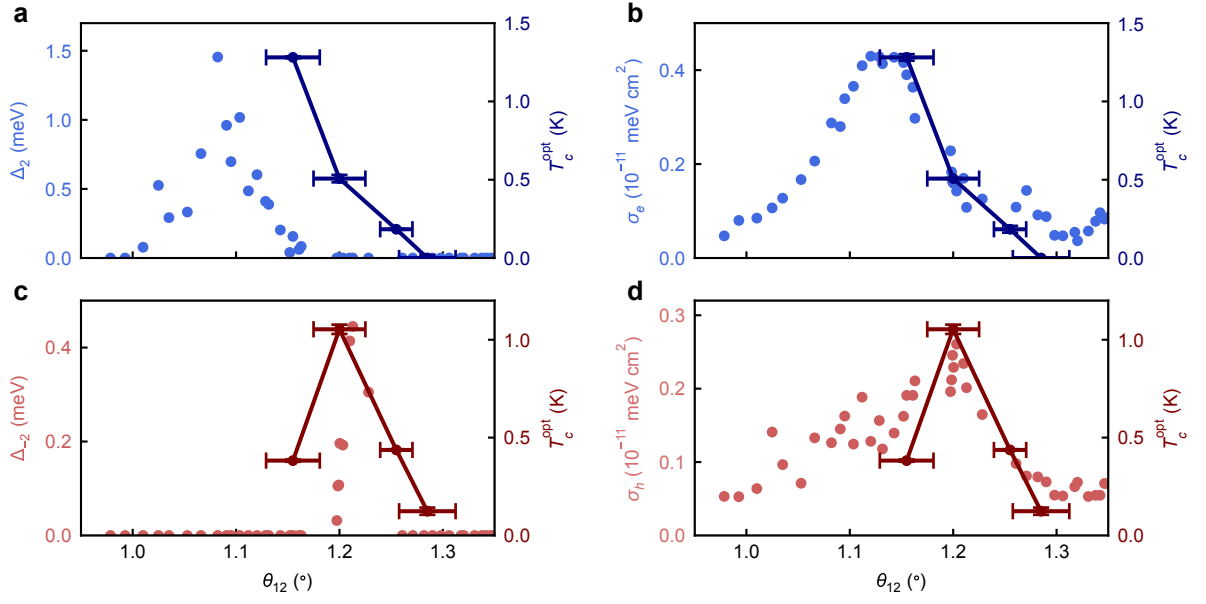


FIG. ED9. **Comparison of compressibility data from the first line cut with transport.** **a**, Gap Δ_2 of the $\nu = 2$ correlated insulator (left axis) as measured from the line cut in Fig. 2 (same as the line cut 1 in Fig. ED3) and optimal critical temperature T_c (right axis) as measured from transport as a function of twist angle θ_{12} . **b**, Strength of the sawtooth compressibility σ_e for the conduction band (left axis) as measured from the line cut and optimal T_c (right axis) as measured from transport as a function of twist angle θ_{12} . **c-d**, Same as **a-b**, but for hole doping.

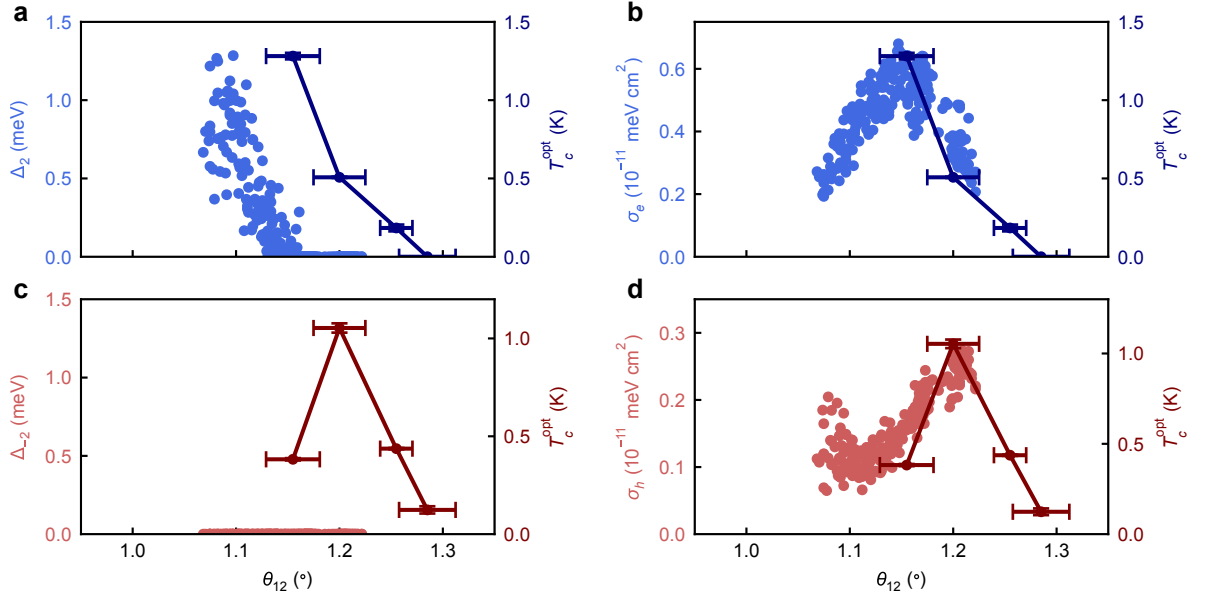


FIG. ED10. **Comparison of compressibility data from the $1 \times 1 \mu\text{m}^2$ grid with transport.** **a**, Δ_2 , measured within the grid (Fig. ED5; left axis) and T_c^{opt} determined from transport measurements (right axis) as a function of θ_{12} . **b**, σ_e measured within the grid (left axis) and optimal T_c^{opt} determined from transport measurements (right axis) as a function of θ_{12} . **c-d**, Same as **a-b**, but for the hole doping.